

Thesis for the degree of Licentiate of Engineering

Microkinetic Modeling of Nanoparticle Catalysis using Density Functional Theory

Mikkel Jørgensen



CHALMERS

Department of Physics
Chalmers University of Technology
Gothenburg, Sweden 2017

Microkinetic Modeling of Nanoparticle Catalysis using Density Functional Theory
Mikkel Jørgensen

© Mikkel Jørgensen, 2017

Department of Physics
Chalmers University of Technology
SE-412 96 Gothenburg
Sweden
Telephone: +46 (0)31-772 1000

Cover:

Kinetic simulations, represented by dices, close the materials gap between extended surfaces and nanoparticles.

Printed at Chalmers Reproservice
Gothenburg, Sweden 2017

Mikkel Jørgensen
Department of Physics
Chalmers University of Technology

Abstract

Heterogeneous catalysis is vitally important to modern society, and one path towards rational catalyst design is through atomistic scale understanding. The atomistic scale can be linked to macroscopic observables by microkinetic models based on first-principles calculations. With the increasing accuracy of first-principles methods and growing computational resources, it has become important to investigate and further develop the methodology of microkinetic modeling, which is the theme of this thesis.

First, a procedure for mean-field microkinetic modeling of reactions over extended surfaces is developed, where complete methane oxidation over Pd(100) and Pd(111) is studied as an example. The model reveals how the main reaction mechanisms depend on reaction conditions, and shows poisoning as well as promotion phenomena.

Second, the effect of entropy in microkinetic modeling is investigated, where CO oxidation over Pt(111) is used as a model reaction. Entropy is found to affect reaction kinetics substantially. Moreover, a method named Complete Potential Energy Sampling (CPES) is developed as a flexible tool for estimating adsorbate-entropy.

Third, a kinetic Monte Carlo method is developed to bridge the materials gap in heterogeneous catalysis. The computational cost to map out the complete reaction-energy-landscape on a nanoparticle is high, which is solved herein using generalized coordination numbers as descriptors for reaction energies. CO oxidation over Pt is studied, and nanoparticles are found to behave differently than the corresponding extended surfaces. Moreover, the active site is found to vary with reaction conditions.

Finally, the reaction orders and apparent activation energies are coupled to the microscale via the degree of rate control, which enhances the atomistic understanding of reaction kinetics.

Keywords: Catalysis, Density Functional Theory, Microkinetic modeling, Nanoparticles, Kinetic Monte Carlo, Mean-field approximation, Entropy, Methane oxidation, CO oxidation.

List of Publications

This thesis is based on the following appended papers:

I.

First-Principles Microkinetic Modeling of Methane Oxidation over Pd(100) and Pd(111)

M. Jørgensen and H. Grönbeck

ACS Catalysis, **6** (2016), 6730-6738

II.

Adsorbate Entropies with Complete Potential Energy Sampling in Microkinetic Modeling

M. Jørgensen and H. Grönbeck

The Journal of Physical Chemistry C, **121** (2017), 7199-7207

III.

Scaling Relations and Kinetic Monte Carlo Simulations to Bridge the Materials Gap in Heterogeneous Catalysis

M. Jørgensen and H. Grönbeck

Accepted, ACS Catalysis, (2017), doi: 10.1021/acscatal.7b01194

IV.

Connection between Macroscopic Kinetic Measurables and the Degree of Rate Control

M. Jørgensen and H. Grönbeck

Submitted, Catalysis Science & Technology, (2017).

My contributions to the publications

Paper I

I programmed the kinetic mean-field code and performed all the calculations. I wrote the first draft of the paper, which was finalized together with my coauthor.

Paper II

I programmed the kinetic mean-field code and performed all the calculations. I wrote the first draft of the paper, which was finalized together with my coauthor.

Paper III

I programmed the kinetic Monte Carlo code and performed all the calculations. I wrote the first draft of the paper, which was finalized together with my coauthor.

Paper IV

I derived the equations, and performed the numerical simulations. I wrote the first draft of the manuscript, which was finalized together with my coauthor.

Contents

1	Introduction	1
1.1	Thesis Objectives	3
2	Calculating Rate Constants	5
2.1	Reaction Rate Constants	5
2.2	Density Functional Theory	6
2.2.1	Exchange Correlation Energy Approximations	8
2.2.2	Projector-Augmented Wave Method	9
2.2.3	Periodic Systems	10
2.3	Local Minimum Energies	11
2.4	Energy Barriers with Nudged Elastic Band	11
2.5	Adsorbate-Adsorbate Interactions	12
2.6	Modeling Entropies in Catalytic Reactions	13
2.7	Summary	15
3	Simulating Reaction Kinetics	17
3.1	Chemical Master Equation	17
3.2	Mean-Field Approximation	18
3.3	Kinetic Monte Carlo	20
3.4	Analyzing Reaction Kinetics	22
3.4.1	Reaction Mechanisms	22
3.4.2	Turnover Frequencies and Coverages	23
3.4.3	Reaction Orders and Apparent Activation Energies	23
3.4.4	Degree of Rate Control	24
3.5	Summary	25
4	Kinetic Models for Methane and CO Oxidation	27
4.1	Constructing a Kinetic Model	27
4.2	Complete Methane Oxidation over Pd(100) and Pd(111)	28
4.3	Entropic Effects in CO Oxidation on Pt(111)	31
4.4	Catalysis on Nanoparticles	33
5	Conclusion & Outlook	37
	Acknowledgments	39

Chapter 1

Introduction

"What would happen if we could arrange the atoms one by one the way we want them ... I can hardly doubt that when we have some control over the arrangement of things on a small scale we will get an enormously greater range of possible properties that substances can have and of different things we can do ... Atoms on a small scale behave like nothing on a large scale, for they satisfy the laws of quantum mechanics." Richard P. Feynman(1959)¹.

This was how Richard Feynman envisioned the influence that nanotechnology will have in society, nearly 60 years ago. Today, his visions of manipulating matter at the atomic scale is close to reality. Systems can be designed atom by atom, which is a consequence of understanding the quantum mechanical behavior of atomic systems. Understanding the behavior of matter at the smallest scale is crucial as it enables rational design, and manipulation, of properties in nanoparticle-based technologies.

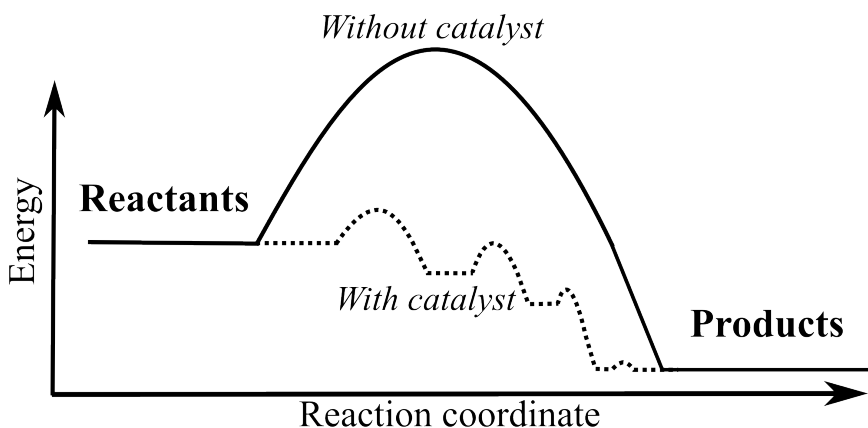


Figure 1.1: Schematic illustration of a catalytic reaction. The catalyst provides an alternative pathway with lower energy barriers for a chemical reaction.

One technology that benefits from atomistic understanding is heterogeneous catalysis. Heterogeneous catalysis has a range of applications in society, such as cleaning automotive exhaust from harmful gases, producing synthetic fuels, and manufacturing chemicals. In the chemical industry, about 90% of the production applies catalysts^{2 (p. 11)}. Because of this, small improvements can have major impacts on a global scale. A catalyst is a substance that speeds up a chemical reaction without being consumed in the process. In Figure 1.1, a catalytic reaction is illustrated, where reactants are converted to products

with lower energies as compared to the case without a catalyst. The conversion of reactants proceeds on the surface of the catalyst, which provides an alternative pathway for the reaction. To maximize the exposed surface area, heterogeneous catalysts are often designed as precious metal-nanoparticles, dispersed on porous metal-oxide supports.

Since catalysis proceeds on the surface of nanoparticles, understanding bonding on surfaces is required. The first step in a catalytic cycle is adsorption of reactants on the surface. Next, the reactants form new chemical bonds mediated by the surface, and finally the resulting products should desorb from the surface. For the catalytic cycle to proceed efficiently, the adsorbate-surface bond should neither be too strong nor too weak. This point is contained in the Sabatier principle² (p. 264), which states that for a given reaction, there is an optimal binding energy of the reactants. The fact that there is an optimal binding energy has led to the recognition that only a few sites might be active in a catalytic reaction and the concept of active sites³. An early description to quantify the rate of a catalytic reaction was the Arrhenius equation² (p. 36), which gives an empirical expression for the rate constant:

$$k = A \exp\left(\frac{-E_a}{k_B T}\right) \quad (1.1)$$

where E_a is the activation energy, A is a pre-exponential factor, and T is the temperature. As E_a appears in the exponent, small variations in E_a results in large changes in the rate. A smaller activation energy allows for a higher efficiency, since the temperature can be kept low. The Arrhenius equation is connected to the Sabatier principle as the activation energy usually is correlated with the bond strengths of the reactants. This is the essence of the Brønsted-Evans-Polanyi (BEP) principle²(p. 267), which states that the transition state energy of a reaction depends on the bond strength of the adsorbates.

Besides the general and phenomenological insights contained in the Sabatier principle and the Arrhenius equation, the microscopic picture of catalysis has been elucidated by the computational chemistry and physics communities. The development of electronic structure calculations; especially Density Functional Theory^{4;5}, have played an important role in studies of catalytic reactions⁶. Some of the earliest models of the catalyst surface were small clusters that locally mimicked the active site⁷. These cluster models are fair approximations to the catalyst surface⁷, which can explain chemical bonds between adsorbates and surfaces qualitatively. Later, when the computational power had matured, slab models were applied to model extended surfaces⁷, which presently is the most common approach. Slab models have enabled quantitative descriptions of the adsorbate-surface bond. Explicit calculations on nanoparticles still pose a special challenge due to the system size and structural complexity. However, during the past few years, studies of adsorption on idealized nanoparticle-models have been conducted using first-principles calculations⁸⁻¹⁷.

In addition to studies of specific reactions, computational approaches have been used to understand trends in catalytic properties. One example is the adsorption on transition metal surfaces, where the leftmost metals in the periodic table of elements are more reactive than the metals to the right. This trend was rationalized by the d-band model¹⁸, where the center and filling of the d-band determines the reactivity of a certain catalyst site. Different sites on nanoparticles have different coordination numbers that correspond

to varying d-band centers. Thus, the d-band model suggests that the coordination number should be a proper descriptor for binding energies⁶. To improve on the coordination number as a descriptor, the coordination numbers of the first nearest neighbor can be taken into account. This was recently realized with the generalized coordination number that was shown to be a good descriptor for the reactivity on extended surfaces and nanoparticles^{19–21}.

Adsorption studies solely account for the thermodynamic aspects of catalysis. However, to fully understand a reaction it is also central to describe the reaction kinetics. The reaction kinetics can be elucidated using a microkinetic model, which is a mathematical representation of a reaction as a set of intermediate steps. The benefit of constructing a microkinetic model is that the main reaction mechanisms and kinetic bottlenecks are accessible, which reveals the elementary steps that should be targeted in future catalyst design. Previously, microkinetic models based on experimental measurements^{22–28} and first-principles calculations^{29–43} have been formulated for various catalytic reactions. Although this field is rapidly growing, the number of formulated microkinetic models is still modest⁴⁴. Models derived from first-principles calculations been formulated using several different methods, and it is timely to investigate and develop the general methodology of microkinetic modeling, especially to take advantage of the growing computational power.

Furthermore in the preceding literature, extended surfaces have often be used as model-systems for nanoparticles. Using extended surfaces gives the benefit of structural simplicity. However, it simultaneously gives rise to a, so-called, materials gap between technical catalysis and model systems. Efforts have previously been made to bridge the materials gap by performing experiments on surfaces and well-defined nanoparticles^{45–48}. Additionally, theoretical models have been constructed to understand the kinetics on nanoparticles^{38;40;49;50}. In these theoretical studies, the considered reaction energy landscapes were simplified or the reactions schematic. Hence, there is a need to understand nanoparticle catalysis using first-principles-based reaction energy landscapes.

1.1 Thesis Objectives

The purpose of this thesis is to investigate and develop the methodology of first-principles microkinetic modeling of reactions on extended surfaces and nanoparticles. In particular, it aims to investigate catalysis through mean-field modeling and kinetic Monte Carlo simulations. Furthermore, methods for analysis of microkinetic simulations and comparison with experimental results are discussed. Special emphasis is placed on the modeling of adsorbate entropy, and how to bridge the materials gap between extended surfaces and nanoparticles.

The necessary components for formulating, solving, and analyzing first-principles microkinetic models are illustrated in Figure 1.2. The first step is to choose a simplified model system of the catalyst. Simplification of the real catalyst is necessary as a technical catalyst is complex and ill-defined. Moreover, working with a simple model system will likely result in a clearer understanding of catalytic mechanisms. The choice of model system can include extended surfaces as well as nanoparticles, which both will be treated in the upcoming chapters. The next ingredient in the modeling is an energy landscape for the reaction, which is the set of Gibbs free energy barriers for the considered elementary

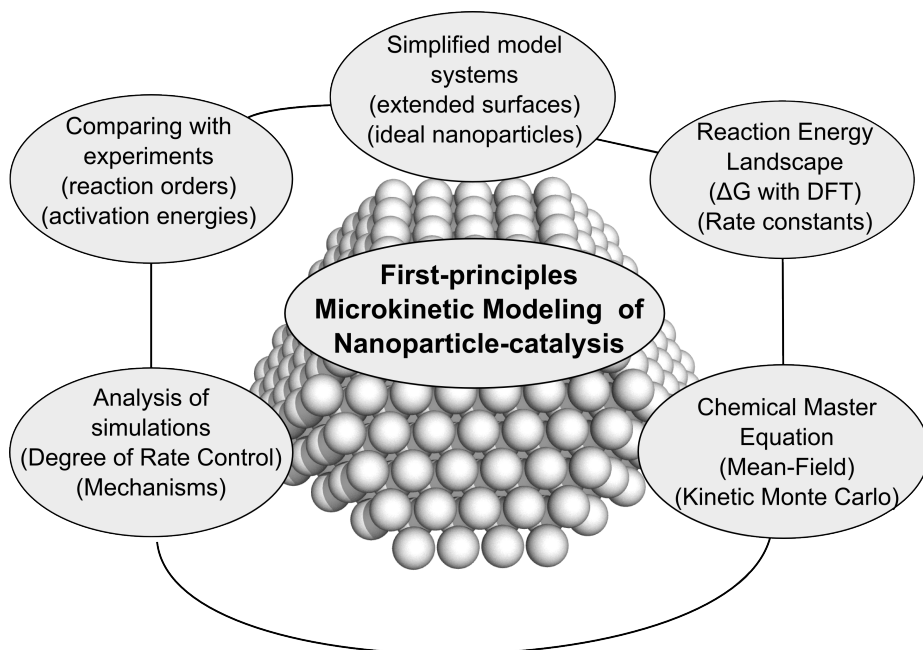


Figure 1.2: Concept map of the thesis. The map illustrates necessary components to model catalysis from first principles.

reactions. All Gibbs free energies in the present work are calculated using Density Functional Theory (DFT). When the Gibbs free energy barriers have been obtained, the rate constants can be calculated. Construction of the reaction energy landscape and rate constants are treated in chapter 2. With access to the rate constants of all elementary reactions, the kinetics can be simulated by solving the chemical master equation. The master equation can in special cases be solved approximately in the mean-field approximation, and when the mean-field approximation is not applicable, the kinetics can be simulated with kinetic Monte Carlo. Kinetic Monte Carlo is necessary to simulate the kinetics of reactions on nanoparticles. Simulation of reaction kinetics and analysis of the results are treated in chapter 3. The results of the kinetic simulations should be analyzed to understand the governing reaction mechanisms and to determine which elementary steps that control the rate. Here, the rate controlling steps are quantified by a degree of rate control analysis. Ultimately, the success of a first-principles microkinetic model depends on how well it agrees with experiments. To compare with experiments, the model can be used to simulate reaction orders and apparent activation energies. Examples of the developed methodologies are presented in chapter 4, which describes kinetic models of methane and CO oxidation.

Chapter 2

Calculating Rate Constants

To simulate reaction kinetics, it is necessary to calculate the rate constants of the elementary steps in the microkinetic model. This chapter deals with calculations of rate constants from first principles using Density Functional Theory.

2.1 Reaction Rate Constants

Rate constants can be estimated using Transition State Theory^{51;52} (TST). The TST rate constant for an elementary reaction is derived by dividing phase-space into a reactant and product region by a specific dividing surface⁵². All points on the dividing surface in phase-space define the transition state (R^\ddagger). Reactants (R) that cross this dividing surface become products (P). The main assumption of TST is that the reactant and transition state are in equilibrium, and that the transition rate into the product region is so low that the Boltzmann distribution remains intact⁵². The second assumption is that the reactants cross the dividing surface only once. Thereby, the TST estimate of the rate constant will always be larger than the actual rate constant. The reaction can be written as:



The TST rate constant is written as a frequency f of the molecules passing R^\ddagger into P , multiplied with the ratio of the partition functions as⁵²:

$$k^{\text{TST}} = f \frac{Z^\ddagger}{Z^R}, \quad (2.2)$$

where Z^\ddagger is the partition function in the transition state and Z^R is the partition function of the reactant state. f can be found using the Maxwell-Boltzmann speed distribution, and assuming that R^\ddagger has a finite width δ , such that $Z^\ddagger = \delta Z^*$. Using this, the rate constant can be shown to take the following form⁵²:

$$k^{\text{TST}} = \frac{k_{\text{B}}T}{\sqrt{2\pi\mu k_{\text{B}}T}} \frac{Z^*}{Z^R}, \quad (2.3)$$

where μ is an effective mass for the reaction coordinate.

An effective mass of the reaction coordinate is an abstract concept, and it is cumbersome to work with. Therefore, it is often assumed that the reaction coordinate is a vibration with frequency ν . Taking the classical limit of the partition function for this vibrational mode, in the limit where $k_{\text{B}}T \gg h\nu$, gives a simple expression for the rate constant⁵¹:

$$k^{\text{TST}} = \frac{k_{\text{B}}T}{h} \frac{Z^\ddagger}{Z^R}. \quad (2.4)$$

For a barrierless adsorption reaction, where the gas-phase reactant molecule impinges on a substrate atom with area A , one can deduce the following expression⁵²

$$k_{\text{ads}}^{\text{TST}} = \frac{s_0 p A}{\sqrt{2\pi M k_B T}}, \quad (2.5)$$

where p is the pressure of the gas, A is the area of the adsorption site, M is the molecule mass, and s_0 is the sticking probability. If this expression is used for the adsorption rate constant, the corresponding desorption rate constant k_{des} can be determined from the equilibrium constant K :

$$K = \frac{k_{\text{ads}}}{k_{\text{des}}} = e^{-\frac{\Delta G}{k_B T}}, \quad (2.6)$$

where ΔG is the Gibbs free energy change upon adsorption. In this manner, thermodynamic consistency is ensured.

The Gibbs free energy change is composed of an enthalpy (ΔH) and an entropy (ΔS):

$$\Delta G = \Delta H - T\Delta S \quad (2.7)$$

The enthalpy change of the reaction is determined by electronic rehybridization, where bonds are broken and new bonds are formed. Likewise, the entropy is determined by the potential energy landscape. Therefore, it is essential to calculate the energy of atomic systems, which can be achieved using Density Functional Theory.

2.2 Density Functional Theory

The total energy of a system of atoms is calculated using the stationary Schrödinger equation:

$$\hat{H}|\Psi\rangle = E|\Psi\rangle, \quad (2.8)$$

where the many-body Hamiltonian \hat{H} can be written:

$$\hat{H} = \hat{H}_{eZ} + \hat{H}_{ee} + \hat{H}_{ZZ}. \quad (2.9)$$

The expression (2.9) includes contributions from electron-nuclei interactions (eZ), electron-electron interactions (ee), and nuclei-nuclei interactions (ZZ). The corresponding Schrödinger equation to (2.9) does not allow an analytical solution for more than one electron, and must be solved by approximations.

One common approximation is the Born-Oppenheimer Approximation, which treats the nuclei with classical physics and invokes the adiabatic approximation. The adiabatic approximation states that electrons move on a much shorter time scale than the nuclei. Therefore, the electrons instantaneously follow the nuclei during atomic motion without undergoing transitions between stationary states. However, the stationary states vary as the nuclei move. The adiabatic approximation holds if the ratio of the electron to nuclei mass is small compared to the energy difference between different adiabatic eigenstates^{53 (p. 9)}. The second part of the Born-Oppenheimer approximation treats nuclei as classical, which can be rationalized due to their large thermal wavelengths (λ_T).

λ_T is roughly the average de Broglie wavelength at a given temperature^{53 (p.10)}. Particles with substantially larger separation than λ_T do not exhibit quantum phase coherence, and the total nuclear wavefunction is simply the product of the individual wavefunctions. When the Born-Oppenheimer approximation is invoked, it is sufficient to deal with the electronic part of the Hamiltonian \hat{h}_e :

$$\hat{h}_e = \hat{T} + \hat{V}_{\text{ext}} + \hat{V}_{ee} = \hat{T}_e + \hat{V}_{\text{ext}} + \hat{V}_H + \hat{V}_{XC} \quad (2.10)$$

Where \hat{T} is the kinetic energy operator for the electrons, \hat{V}_{ext} is the external classical electrostatic field set up by the nuclei, and \hat{V}_{ee} describes the electron-electron interactions. In the second equality \hat{V}_{ee} is split up into the classical Hartree energy \hat{V}_H and the quantum mechanical exchange and correlation energy \hat{V}_{XC} . The Hartree energy is simply the electrostatic energy of the field set up by the electrons, which has a non-physical self-interaction that should be canceled by \hat{V}_{XC} .

The exchange energy stems from the indistinguishability principle and symmetrization postulate of quantum mechanics, which state that a fermionic wavefunction is anti-symmetric under particle permutation. These constraints modify the electronic energy with the so-called exchange energy. Exchange will make electrons of identical spin less likely to be close as two fermions cannot occupy the same quantum state. The correlation energy is the energy related to correlation of electronic motion. In this sense, exchange interaction is also a form of correlation.

Density Functional Theory is based on the two Hohenberg-Kohn (HK) theorems⁴. The first HK theorem states that the ground state electronic density (ρ) uniquely determines the external potential (\hat{V}_{ext}). This implies that ρ also determines the ground state $|\Psi\rangle$ of the many body problem. The second HK theorem defines the variational energy as a functional of ρ ⁴

$$E_v[\rho] = \langle \Psi[\rho] | \hat{T} + \hat{U}_{ee} | \Psi[\rho] \rangle + \int \rho(\mathbf{r}) v_{\text{ext}}(\mathbf{r}) \, d\mathbf{r} \quad (2.11)$$

Where v_{ext} is the external potential. It must be noted that Ψ depends on ρ and vice versa, which implies that the problem must be solved self-consistently.

The expression for the kinetic energy of the real interacting system is unknown as a functional of the density. This difficulty is circumvented in the Kohn-Sham scheme⁵, where one works with a fictitious non-interacting system that has the same density as the real system. The benefit is that the ground state of a non-interacting system is simply the Slater-determinant composed of the individual single particle states. In the fictitious reference system, the Hamiltonian is^{53 (p. 61)}

$$\hat{H}_R = \sum_{i=1}^N \left(\hat{T}_R + v_R(\mathbf{r}_i) \right) \quad (2.12)$$

Where N is the number of electrons. The first term is the single particle non-interacting kinetic energy operator, and v_R is a reference potential which ensures that the density coincides with the density of the interacting system. v_R can be derived using variational calculus with the constraint that ρ integrates to N ; this yields^{53 (p. 63)}

$$v_R(\mathbf{r}) = v_{\text{ext}}(\mathbf{r}) + \int \frac{\rho(\mathbf{r}')}{|\mathbf{r} - \mathbf{r}'|} \, d\mathbf{r}' + \frac{\delta \tilde{E}_{XC}}{\delta \rho(\mathbf{r})}. \quad (2.13)$$

The second term in (2.13) is the Hartree energy and the third term is a chemical potential, which is formulated as a functional derivative with respect to ρ . \tilde{E}_{XC} is a modified exchange-correlation energy that must be introduced when neglecting kinetic correlations in the reference system. The Kohn-Sham equations are a set of equations defined by (2.12). These equations must be solved self-consistently since v_R depends on ρ and vice-versa. Finally, the energy is evaluated by the Kohn-Sham functional^{53 (p. 62)}

$$E_{KS}[\rho] = T_R + \int \rho(\mathbf{r})v_{\text{ext}}(\mathbf{r}) \, \mathbf{d}\mathbf{r} + \frac{1}{2} \iint \frac{\rho(\mathbf{r})\rho(\mathbf{r}')}{|\mathbf{r} - \mathbf{r}'|} \, \mathbf{d}\mathbf{r}\mathbf{d}\mathbf{r}' + \tilde{E}_{XC}[\rho] \quad (2.14)$$

The only remaining unknown quantity here is the exchange-correlation energy, which determines the accuracy of DFT. It is interesting to note that DFT is an exact theory, given the true exchange-correlation energy.

2.2.1 Exchange Correlation Energy Approximations

The approximation of the exchange-correlation functional is a major concern when it comes to the accuracy of DFT. One can view the exchange-correlation energy as the Coulomb interaction between the density and a displaced charge density, which is brought about by exchange and correlation^{53 (p. 69)}. This displaced charge density is called the exchange-correlation hole $\tilde{\rho}_{XC}(\mathbf{r}, \mathbf{r}') = \rho(\mathbf{r}') [g(\mathbf{r}, \mathbf{r}') - 1]$. Here $g(\mathbf{r}, \mathbf{r}')$ is the pair-correlation function, describing the probability to find an electron at \mathbf{r} given that one is already present at \mathbf{r}' .

The simplest and earliest kind of exchange-correlation approximation is the Local Density Approximation (LDA)⁵. In LDA, the exchange-correlation is approximated by considering the inhomogeneous electron gas as being locally homogeneous, thus applying the exchange-correlation hole of the homogeneous electron gas. In this way, the exchange-correlation energy is found by integration with an energy density $\tilde{\epsilon}_{XC}^{\text{LDA}}$:

$$\tilde{E}_{XC}^{\text{LDA}}[\rho] = \int \rho(\mathbf{r})\tilde{\epsilon}_{XC}^{\text{LDA}}[\rho(\mathbf{r})] \, \mathbf{d}\mathbf{r}. \quad (2.15)$$

The exchange-correlation hole and pair-correlation function for an inhomogeneous electron gas is however non-local. To introduce some semi-local behavior and improve on LDA, the Generalized Gradient Approximation (GGA) can be invoked^{53 (p. 86)}. This approximation improves over LDA by taking into account the gradient of the density. GGA functionals are constructed by augmenting the LDA energy density with an exchange-correlation enhancement factor $F_{XC}[\rho]$. Thereby the exchange-correlation energy becomes

$$\tilde{E}_{XC}^{\text{GGA}}[\rho] = \int \rho(\mathbf{r})\tilde{\epsilon}_{XC}^{\text{LDA}}[\rho(\mathbf{r})]F_{XC}[\rho(\mathbf{r}), \nabla\rho(\mathbf{r})] \, \mathbf{d}\mathbf{r}. \quad (2.16)$$

Multiple GGA functionals have been developed throughout time, and one popular choice is the Perdew-Burke-Ernzerhof (PBE) functional⁵⁴. Another GGA functional derived from PBE is the revised PBE functional of Hammer et al.⁵⁵ (RPBE), which is optimized for chemisorption. Metallic systems are generally well described using PBE, whereas chemisorption problems might prove more difficult. For example, PBE predicts the lattice

constant of Pd to be⁵⁶ 3.99 Å, and RPBE gives 4.02 Å. Experiments give⁵⁶ a lattice constant of 3.876 Å, and PBE comes closer to the experimental lattice constant. PBE predicts the chemisorption energy of CO on Pd(111) at the fcc site to be⁵⁵ -1.94 eV, whereas RPBE yields -1.65 eV. The corresponding experimental value is⁵⁵ -1.47 eV. Similar improvements for RPBE over PBE in the chemisorption energy exist for oxygen⁵⁵. This indicates that PBE performs better for the solid, whereas RPBE predicts good chemisorption energies. In microkinetic modeling the chemisorption energies are most important as lattice-parameters do not enter the rate constant calculations explicitly. Therefore, the RPBE functional is applied in Paper II and Paper III to model CO oxidation over Pt.

The exchange-correlation energy of GGA functionals can be improved further, and different strategies exist^{53 (chap. 5)} such as, meta-GGAs, van der Waals functionals, and hybrid functionals where exact exchange energies are included.

The discussion concerning DFT is straightforwardly generalized to spin-polarized systems. This is done by decomposing ρ into a spin-up density and a spin-down density ($\rho = \rho_{\uparrow} + \rho_{\downarrow}$), where one must solve the Kohn-Sham equations for each spin channel separately.

2.2.2 Projector-Augmented Wave Method

When performing DFT calculations in practice, a certain basis set is needed to represent the Kohn-Sham orbitals. In the present work, the applied basis functions are plane waves. Plane waves are advantageous for periodic systems as they fulfill Bloch's theorem^{53 (p. 129)}. Another advantage is that increasing the number of plane wave components in the basis results in monotonous convergence of the energy. Other choices of basis functions include numerical grids and atomic orbitals^{53 (chap. 8)}.

The wavefunctions close to the nuclei oscillate rapidly due to orthogonality, and it would require an unreasonable plane-wave basis to describe these oscillations. To avoid describing the oscillations explicitly, the Projector-Augmented Wave (PAW) method⁵⁷ is used. In PAW, the core electrons are usually treated as chemically frozen as they do not directly take part in the rehybridization, and only the valence electrons are treated explicitly. The valence wavefunctions are treated by introducing a linear transformation \mathcal{T} between the true wavefunction $|\Psi\rangle$ and a pseudo wavefunction $|\tilde{\Psi}\rangle$. Real-space is divided up into interstitial regions between the atomic cores and augmentation regions around the cores. The pseudo wavefunction is chosen to be a smooth function inside augmentation regions, which needs a smaller basis set. The method requires that $|\tilde{\Psi}_i\rangle = |\Psi_i\rangle$ outside the augmentation regions, and that they match in value and derivative at the boundary. The transformation \mathcal{T} only acts locally in each augmentation region, and it is the identity transformation outside.

The transformation is performed using different basis functions than plane-waves. This basis functions can be the all-electron partial waves $|\phi_i\rangle$, which are found by integration of the radial part of the Schrödinger Equation for the isolated atom. Here i denotes all angular momentum quantum numbers and an index labeling the atom in question. i also contains an index n that describes different partial waves for identical angular momenta and atomic sites. Each $|\phi_i\rangle$ is assigned a pseudo partial wave $|\tilde{\phi}_i\rangle$ that is equal to $|\phi_i\rangle$

outside of the augmentation region. $|\tilde{\phi}_i\rangle$ forms a complete set inside. Using the partial waves as basis functions inside the augmentation regions, the transformation takes the form⁵⁷

$$\begin{aligned}\mathcal{T} &= I + \sum_i \left(|\phi_i\rangle - |\tilde{\phi}_i\rangle \right) \langle \tilde{p}_i| \\ |\Psi\rangle &= \mathcal{T} |\tilde{\Psi}\rangle\end{aligned}\quad (2.17)$$

Where I is the identity operator and $\langle \tilde{p}_i|$ is a projector function. There is one $\langle \tilde{p}_i|$ for each $|\tilde{\phi}_i\rangle$, which fulfill the conditions:

$$\sum_i |\tilde{\phi}_i\rangle \langle \tilde{p}_i| = I, \quad \langle \tilde{p}_i | \tilde{\phi}_j \rangle = \delta_{ij}.$$
 (2.18)

It should be noted that the projectors are local operators inside each augmentation region that project out the relevant part of the wavefunction. Hence, inside an augmentation region the wavefunction is the augmented part of the sum in (2.17), whereas outside the projectors are orthogonal to $|\tilde{\Psi}\rangle$ and no augmentation takes place.

2.2.3 Periodic Systems

The atomistic model systems in the present work were chosen to be periodic systems. The wavefunction of an electron in a periodic potential ($\psi_{\mathbf{k}}$) obeys Bloch's theorem, which can be stated as^{53 (p. 129)}

$$\psi_{\mathbf{k}}(\mathbf{r}) = e^{i\mathbf{k}\cdot\mathbf{r}} u_{\mathbf{k}}(\mathbf{r}),$$
 (2.19)

where \mathbf{k} is the wavenumber and $u_{\mathbf{k}}$ is a function with the periodicity of the potential. Using the periodic zone scheme^{58 (p. 223)} and working in the first Brillouin zone, the wavefunction of an infinite solid is described taking only one unit-cell into account. In principle, all possible wavenumbers must be included in the calculation, however in practice this is solved by Brillouin zone sampling. In Brillouin zone sampling, one represents the density, hence the energy, as a sum over special wavenumbers in the first Brillouin zone called k-points:

$$\rho(\mathbf{r}) = \sum_{\mathbf{k} \in \text{BZ}} \omega_{\mathbf{k}} |\psi_{\mathbf{k}}(\mathbf{r})|^2$$
 (2.20)

Where $\omega_{\mathbf{k}}$ are weights that depend of the symmetry of the Brillouin zone. In practice, symmetry is applied and only points in the irreducible wedge of the Brillouin zone are considered. The density is given as a sum over each k-point as

$$\rho(\mathbf{r}) = \sum_{\mathbf{k} \in \text{BZ}} \omega_{\mathbf{k}} \sum_{i=1}^{N_{\mathbf{k}}} f_i^{(\mathbf{k})} |\phi_i^{(\mathbf{k})}(\mathbf{r})|^2,$$
 (2.21)

where $\phi_i^{(\mathbf{k})}(\mathbf{r})$ are the eigenstates of the Kohn-Sham equations, $f_i^{(\mathbf{k})}$ are the occupation numbers of the orbitals, and $N_{\mathbf{k}}$ is the number of occupied electronic states with wavenumber \mathbf{k} . It is necessary to solve a set of coupled Kohn-Sham equations, one for each k-point. The number of k-points is a quantity, which must be increased until convergence in the

quantity of interest is achieved. Furthermore, it should be noted that a larger supercell will require fewer k-points for convergence as a larger unit-cell will result in a smaller Brillouin zone.

When calculating the density it can have practical relevance to work with partial occupation numbers, which is referred to as smearing of the Fermi surface. For metallic systems, this might be necessary as different k-points can make new bands enter or exit the calculation during the self-consistent solution of the Kohn-Sham equations.

2.3 Local Minimum Energies

The previous sections have described how the energy of an atomistic system can be obtained given the atomic positions. However, the precise positions that correspond to local energy minima are generally not known. Energy minima are important to find, since a system will spend a major part of its time near the minima. The local optimization procedure used in this thesis is the Broyden-Fletcher-Goldfarb-Shanno (BFGS) algorithm⁵⁹. The BFGS algorithm is of the Quasi-Newton type where the atomic positions are updated according to the Hessian matrix.

Calculating adsorption energies is done in a series of steps. First, the bulk unit-cell is used to calculate the lattice constant that corresponds to the lowest energy, for example by fitting an equation of state. Next a surface slab is constructed, where the number of layers required to converge the surface- or adsorption-energy is determined. Then adsorbates are placed over sites on the surface, and the system is relaxed locally. There can be multiple local minima on a surface, and each possible minimum should be probed to find the lowest energy. The calculations should also be converged with respect to simulation cell size. Furthermore, a vacuum layer is introduced perpendicular to the surface to avoid interactions between periodic repetitions of the system. For gas-phase molecules, a large cell is required to avoid interactions between periodic repetitions of the system.

Vibrations of gas-phase molecules and adsorbates can also be calculated with DFT. This is often done by assuming a harmonic potential and finding the vibrational frequencies using finite differences. The vibrations become important when analyzing transition states as well as correcting the bare DFT energies for zero-point motion. A zero-point energy is present for confined matter since it defines a Δx in Heisenberg's uncertainty principle. Thereby a small Δx implies a larger Δp , which is responsible for the zero-point energy.

2.4 Energy Barriers with Nudged Elastic Band

The energy barrier for moving a system from the initial state to the transition state plays a central role in describing chemical reactions. The transition state energy is needed to calculate the rate constants. Nudged Elastic Band⁶⁰ (NEB) is a method to find the Minimum Energy Path (MEP) between an initial state and final state, and NEB is also used to identify the transition state.

To initialize a NEB calculation, the initial and final atomic positions are specified. Next, the atomic positions are interpolated between the initial and final state. The resulting atomic configurations are called images, and the distance between the images are described by a reaction coordinate r . Structural optimization is done on each image,

which is connected to the other images by modifying the force component parallel to the MEP. The total force on each image is decomposed in parallel and perpendicular components as:

$$F = F_{\parallel} + F_{\perp} = -kr + F_{\perp} \quad (2.22)$$

where k is a spring constant. Hence, each image interacts with its neighbor images by a spring-force parallel to the MEP, which prohibits full relaxation of each image down to a local minimum (initial or final state). The perpendicular component ensures that each image relaxes down to the MEP at the given reaction coordinate. In this manner, the images are stretched along the MEP.

Typically, the transition state is not found without releasing the highest energy image from all spring forces, and reversing the true parallel force component. As a result, the image climbs up the MEP to the true transition state. This procedure is called the Climbing Image method⁶⁰, which can be switched on after a coarse initial NEB calculation. Whether the highest energy point is a saddle point on the MEP can be verified by vibrating the highest energy image. If the image has one imaginary frequency in the direction of the reaction coordinate, the image is a saddle point on the energy surface and can be considered a transition state.

2.5 Adsorbate-Adsorbate Interactions

The adsorbates on a catalyst surface interact either by direct interactions or by modification of the surface electronic structure^{61;62}. Such phenomena can have large effects on the binding energies of certain species and consequently may be important for the kinetics. A microkinetic model should take this into account by modifying the energies as a function of the adsorbate configurations. Paper I treats adsorbate-adsorbate interactions as functions of the adsorbate coverages, where the energies of the most abundant species (O, C, CO) are perturbed linearly using calculations of the differential adsorption energies. This turns out to be important for obtaining reasonable coverages. In Paper II, an exponential relation is fitted for the CO-CO and O-O interactions, whereas the CO-O interactions are modified linearly. It is important to use the differential adsorption energies instead of the average adsorption energies, as adding another adsorbate will alter the energy of the system based on the adsorbates that are already present.

Adsorbate-adsorbate interactions can also be fitted to specific atomic arrangements. This is achieved by so-called cluster expansion Hamiltonians^{63 (p. 94)} where one calculates the energies of certain geometric occupation-patterns and fits a Hamiltonian to the system. The expansion is truncated at a certain number of nearest neighbors, typically including two and three-particle interactions. In Paper III, the adsorbate-adsorbate interactions are considered between the first nearest-neighbors, and two-particle interactions are accounted for.

Figure 2.1 shows simulated coverages plotted as a function of temperature for complete methane oxidation over Pd(100) using the microkinetic model of Paper I. The applied model includes O-O, C-C, and OH-OH interactions. The figure shows coverages when the interactions are turned off and are at full strength. Without any interactions, O has a very high coverage and there is no C on the surface. At full interaction strength, there is

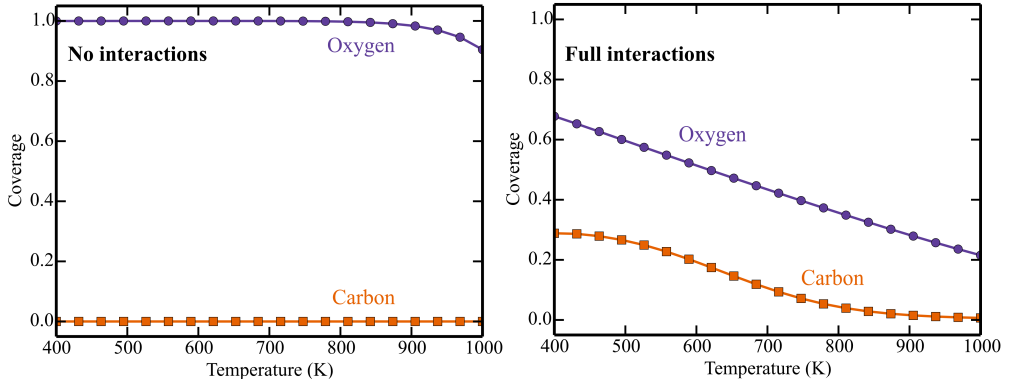


Figure 2.1: Simulated coverages without adsorbate-adsorbate interactions (left) and with adsorbate-adsorbate interactions (right) during complete methane oxidation over Pd(100). Pressures: 0.61 mbar methane and 3.06 mbar oxygen.

a coverage of both C and O. Thus, the adsorbate-adsorbate interactions are of utmost importance for obtaining reasonable coverages and kinetics.

2.6 Modeling Entropies in Catalytic Reactions

The Gibbs free energies entering the rate constants are composed of an enthalpic contribution and an entropic part. Thus, to compute rate constants, the entropy difference between the initial and transition state must be modeled.

To model entropy, it is customary to work in the canonical ensemble and thereby use the canonical partition function Z , which is a sum over all states, available to the system. The entropy and partition function are related by the connection between statistical mechanics and thermodynamics⁶⁴

$$S = -\frac{\partial}{\partial T} (-k_B T \ln Z)_{V,N} = k_B \ln Z + k_B T \frac{1}{Z} \left(\frac{\partial Z}{\partial T} \right)_{V,N}. \quad (2.23)$$

In this way, the entropy is uniquely defined by the partition function.

The partition function of an ideal-gas molecule can be split up into translations, rotation, and vibrations. Assuming that these degrees of freedom are independent, the partition function is a product of the individual contributions:

$$Z = Z_{\text{trans}} Z_{\text{rot}} Z_{\text{vib}}. \quad (2.24)$$

The translational part of the partition function of the free-gas molecule is given by^{2 (p.89)}

$$Z_{\text{trans}} = V \left(\frac{2\pi M k_B T}{h^2} \right)^{3/2}, \quad (2.25)$$

where V is the volume of the gas, and M is the mass. V is often substituted for the pressure using the ideal gas equation of state $pV = k_B T$.

The rotational partition-function can be calculated in the rigid-rotor approximation² (p. 92):

$$Z_{\text{rot}} = \frac{1}{\sigma} \left(\frac{8\pi^2 k_{\text{B}} T}{h^2} \right)^{3/2} \sqrt{\pi I_A I_B I_C} \quad (2.26)$$

where I_X is the moment of inertia of the molecule around the principal axis X , and σ is the symmetry factor of the molecule.

Finally, the vibrational partition function in the Harmonic Approximation has the following form² (p. 90)

$$Z_{\text{vib}} = \prod_i \frac{e^{-\frac{\hbar\omega_i}{2k_{\text{B}}T}}}{1 - e^{-\frac{\hbar\omega_i}{k_{\text{B}}T}}}, \quad (2.27)$$

where ω_i is the vibrational frequency of mode number i . The Harmonic Approximation assumes that the molecule is subject to a parabolic potential leading to the harmonic oscillator energies $\hbar\omega_i$, which can be calculated using finite differences in the energies obtained with DFT.

The partition function of adsorbates differs from gas-phase molecules. Paper II explores the effect of adsorbate entropy in microkinetic modeling. In this context, the method of Complete Potential Energy Sampling (CPES) is developed to estimate adsorbate entropy with DFT. Four different adsorbate entropy approximations were compared in Paper II: the Harmonic Approximation, the Hindered Translator, the Free Translator, and CPES. These approximations differ in the description of the translational partition function parallel to the surface. All remaining degrees of freedom are described as frustrated vibrations.

In the Harmonic Approximation, the adsorbate fixed to one site and subject to a harmonic potential. Thereby all modes are frustrated vibrations, and (2.27) determines the full partition function. If low-energy modes are found ($< 100 \text{ cm}^{-1}$), it can be necessary to truncate the value, as low-energy modes are computationally uncertain.

The Hindered Translator^{65;66} allows for motion of the adsorbates, depending on their diffusion barriers. The model is simple as it ignores surface topology by only treating the fastest path of diffusion. In the Hindered Translator, the adsorbate is subject to a sinusoidal potential, and the two surface-parallel directions are treated with the following partition function⁶⁶:

$$Z_T^{\text{HT}} = \frac{N_{\text{sites}} \frac{\pi r_x}{T_x} \exp\left(-\frac{r_x + 1}{T_x}\right) I_0^2\left(\frac{r_x}{2T_x}\right) \exp\left(\frac{2}{(2 + 16r_x)T_x}\right)}{\left[1 - \exp\left(-\frac{1}{T_x}\right)\right]^2}. \quad (2.28)$$

$T_x = k_{\text{B}}T/h\nu_x$ is the ratio between the thermal energy and the vibrational energy, and $r_x = W_x/h\nu_x$ is the ratio between the diffusion barrier W_x and the vibrational energy. N_{sites} is the number of surface sites, and I_0 is the zero-order modified Bessel function of the first kind, arising from the periodic potential. The last exponential in (2.28) is accounting for zero-point energy corrections⁶⁶. There can be some uncertainties in working with

the Hindered Translator. For example, it treats surface symmetry in a rough way by assuming that the potential energy surface for diffusion obeys $V(x, y) = V(x) + V(y)$, which is questionable for most surfaces. The Hindered Translator is, however, expected to be accurate for closed-shell molecules due to the presumably flat energy landscape for diffusion.

The Free Translator is derived by assuming completely free diffusion of the adsorbate over the surface. The translational partition function is given by that of a 2D free-gas:

$$Z_{\text{trans}}^{\text{Free}} = A \frac{2\pi M k_{\text{B}} T}{h^2}, \quad (2.29)$$

where A is the area that the adsorbate is free to translate over. The free translator defines an upper bound to the translational entropy of any adsorbate as it corresponds to a completely flat potential energy landscape.

CPES is developed in Paper II as an alternative method for calculating entropies. The method uses DFT calculations to map out the potential energy as a function of adsorbate position in the unit-cell. The translational partition function is evaluated by numerical integration of a semi-classical partition function⁶⁴:

$$Z_{\text{trans}}^{\text{CPES}} = \frac{2\pi M k_{\text{B}} T}{h^2} \iint e^{\frac{-V(x, y)}{k_{\text{B}} T}} dx dy, \quad (2.30)$$

where $V(x, y)$ is the potential energy of the molecule at position (x, y) in the unit-cell. $V(x, y)$ is calculated with DFT by locally optimizing the adsorbate in the direction perpendicular to the surface, for various (x, y) . For a completely flat potential energy surface with $V(x, y) = 0$, (2.30) coincides with the Free Translator partition function (2.29). The CPES method takes the surface symmetry into account as well as the detailed potential energy landscape. In this sense, the CPES method is as accurate as the chosen exchange-correlation potential used in the DFT calculations. Rotations can also be modeled using (2.30) by mapping out a potential energy surface for rotation over some angle θ , and evaluating the integral over θ . However, a complication is that the potential energy for rotations and translations over a surface may be mutually dependent, which can be solved by treating translations and rotations together using (2.30) and mapping out $V(x, y, \theta)$.

The approximations discussed in this section are only valid in the low coverage limit as they do not include adsorbate-adsorbate interactions. However, CPES can include the effect of adsorbate-adsorbate interactions by reformulating (2.30) as a multi-dimensional integral over multiple atoms by mapping out a potential $V(x_1, y_1, x_2, y_2, \dots)$.

2.7 Summary

This chapter has described how rate constants can be calculated by DFT. To describe the Gibbs free energy properly, modeling of adsorbate-adsorbate interactions and entropy calculations were also discussed. The uncertainties in calculating rate constants primarily come from the uncertainty in the DFT calculations, the approximate treatment of

adsorbate-adsorbate interactions, and approximations made to the entropy. DFT calculations and adsorbate-adsorbate interactions give a large contribution to the uncertainty, whereas entropy has a slightly lower impact.

Chapter 3

Simulating Reaction Kinetics

The previous chapter described how to calculate the rate constants of catalytic reactions, which are determined by Gibbs free energies. The present chapter deals with simulating and analyzing reaction kinetics, where the discussion begins with the chemical master equation.

3.1 Chemical Master Equation

The kinetics of a chemical reaction can be viewed as a set of transitions of a system into various states. Reactions occur on a high-dimensional free energy surface with several maxima and minima. In principle, a reaction can be followed in space and time by solving Newton's equations of motions with molecular dynamics. However, molecular dynamics is unfeasible for simulations of reaction kinetics, as the time-step is several orders of magnitude smaller than the typical time of a chemical reaction. This is due to the fact that molecular dynamics spends most time simulating vibrations.

The chemical master equation takes advantage of the time-scale separation between vibrations and chemical reactions by dividing phase-space into regions corresponding to different chemical states of the system. Consider two states of the system: α and β . The chemical master equation connected to state α is given by^{63 (p. 31)}:

$$\frac{dP_\alpha}{dt} = \sum_{\beta} [W_{\alpha\beta}P_\beta - W_{\beta\alpha}P_\alpha], \quad (3.1)$$

where $W_{\alpha\beta}$ is the transition rate from β to α , and P_α is the probability for the system to be in α . The sum in (3.1) runs over all states β , which can bring the system into state α . In practice, the state is often defined by the coverages on the catalyst sites. Thereby, α can be represented as

$$\alpha = \{A^*, B^*, *, *, A^*, *, A^*, B^*, \dots\} \quad (3.2)$$

Where A and B are chemical species, and $*$ denotes an empty site. The set is simply the species occupying the sites of the system. The chemical master equation is the key to the kinetics of the system as it describes the time-evolution for the probability of observing the different states. A high transition rate into a particular state and a low transition rate out of the state, implies that its probability increases in time. Thus, the kinetics will follow the fastest set of transitions into a set of most probable states, which defines the equilibrium.

At equilibrium, one interesting feature of the master equation is that $\frac{dP_\alpha}{dt} = 0$. In this case, $W_{\alpha\beta}P_\beta(t_0) = W_{\beta\alpha}P_\alpha(t_0)$, where t_0 is a time at equilibrium. This is known as

the principle of detailed balance, which reflects that each step is in equilibrium with its own inverse.

3.2 Mean-Field Approximation

The Mean-Field Approximation (MFA) yields an approximate solution to the chemical master equation. To derive the MFA, consider a model surface reaction $A + B \rightarrow AB$. The average number of species A on the surface is given by^{63 (p. 105)}:

$$\langle N_A \rangle = \sum_{\alpha} P_{\alpha} N_{\alpha}^{(A)} \quad \Rightarrow \quad \frac{d\langle N_A \rangle}{dt} = \sum_{\alpha} \left(\sum_{\beta} [W_{\alpha\beta} P_{\beta} - W_{\beta\alpha} P_{\alpha}] \right) N_{\alpha}^{(A)}, \quad (3.3)$$

where $N_{\alpha}^{(A)}$ is the number of species A in state α , and P_{α} is the probability of the system to be in state α . The time-derivative was inserted from the master equation (3.1). The indices of summation can be rearranged to yield^{63 (p. 111)}:

$$\frac{d\langle N_A \rangle}{dt} = \sum_{\alpha} \sum_{\beta} [N_{\alpha}^{(A)} - N_{\beta}^{(A)}] P_{\beta} W_{\alpha\beta} \quad (3.4)$$

For a reaction $A + B \rightarrow AB$, let α correspond to a state with AB , and β corresponds to a state with $A + B$. Then it must hold that $N_{\alpha}^{(A)} - N_{\beta}^{(A)} = -1$. Additionally, given α , then for each β a well-defined number of terms in the sum have non-zero $W_{\alpha\beta}$. This number is equal to the number of adjacent A+B pairs on the surface ($N_{\beta}^{(AB)}$). With the transition rate assumed equal for each β , one obtains^{63 (p. 112)}:

$$\frac{d\langle N_A \rangle}{dt} = \sum_{\beta} -P_{\beta} W N_{\beta}^{(AB)} = -W \langle N^{(AB)} \rangle \quad (3.5)$$

The MFA assumes that the adsorbates are randomly distributed. In this case, the number of pairs in state β becomes^{63 (p. 112)}:

$$N_{\beta}^{(AB)} = Z N_{\beta}^{(A)} \frac{N_{\beta}^{(B)}}{S-1}, \quad (3.6)$$

where Z is the number of nearest neighbors, S is the number of surface sites, and $N_{\beta}^{(B)}/S-1$ is the probability for a site to be occupied by B. Inserting (3.6) into (3.5) gives:

$$\frac{d\langle N_A \rangle}{dt} = \sum_{\beta} -P_{\beta} W Z N_{\beta}^{(A)} \frac{N_{\beta}^{(B)}}{S-1} = -\frac{WZ}{S-1} \langle N^{(A)} N^{(B)} \rangle. \quad (3.7)$$

The mean of a product can be written as the product of the means augmented with the fluctuations from the individual means:

$$\langle N^{(A)} N^{(B)} \rangle = \langle N^{(A)} \rangle \langle N^{(B)} \rangle + \langle [N^{(A)} - \langle N^{(A)} \rangle] [N^{(B)} - \langle N^{(B)} \rangle] \rangle. \quad (3.8)$$

In the limit of an infinite number of sites, $S - 1 \approx S$, and fluctuations can be neglected which gives:

$$\frac{d\langle N_A \rangle}{dt} = -\frac{WZ}{S} \langle N^{(A)} \rangle \langle N^{(B)} \rangle \quad (3.9)$$

Dividing by the number of sites, we find the mean-field equation for the time-evolution of A :

$$\frac{d\theta_A}{dt} = -k\theta_A\theta_B, \quad k = WZ, \quad (3.10)$$

where θ_i is the coverage of species i on the surface, and k is identified as the rate constant of the reaction. Similar equations can be derived for θ_B and the fraction of empty sites. The two main assumptions of the MFA are that the surface is infinite, and that adsorbates are randomly distributed. θ_A corresponds to the probability for observing species A on a surface site. The random distribution implies that configurational entropy is accounted for in the mean-field equations. The assumption that the surface is infinite ($S \gg 1$) breaks down for nanoparticles, where fluctuations cannot be neglected. Moreover, the MFA breaks down for strong adsorbate-adsorbate interactions, and the situation is particularly severe for attractive interactions that lead to pairing of adsorbates.

The advantages of the mean-field picture is that it focuses on the average behavior of the system by describing the coverages. This means that results often are simple to analyze, and that the computational cost of mean-field modeling is considerably smaller than Monte Carlo simulations as the mean-field equations often can be solved on a desktop computer within some minutes. The disadvantage of the MFA is the limitation to infinite surfaces. Furthermore, when working with coverages spacial information is lost, which can be central to understand a reaction mechanism.

In practice, a mean-field model is constructed by having a list of coverages (θ) for species that may cover the surface, and a set of reactions with rates $R(\theta)$. From this information, a system of coupled first-order ordinary differential equations is formulated:

$$\frac{d\theta_i}{dt} = \sum_j c_{ij} R_j(\theta), \quad (3.11)$$

where c_{ij} is an integer that describes how many i -species that are produced in reaction j . R_j is the rate of the elementary reaction j , which is equal to the rate constant times the relevant coverages. As an example, consider the following schematic reaction:



The time-evolution of the coverage of A is given by:

$$\frac{d\theta_A}{dt} = 2k_a^+ \theta_*^2 - 2k_a^- \theta_A^2 - k_c^+ \theta_A \theta_B \quad (3.12)$$

where k_i^\pm is the rate constants for reaction i , and $*$ indicates an empty site. The first term comes from the forward-reaction of (a), which requires two sites for dissociation such that

θ_* enters squared. The factor two is present as two A are formed upon adsorption. The second term stems from the backward reaction of (a). It is negative as A is consumed by the elementary step. The third term arises from reaction (c), which requires one A and B .

For species B the coverage equation is:

$$\frac{d\theta_B}{dt} = k_b^+ \theta_* - k_b^- \theta_B - k_c^+ \theta_A \theta_B. \quad (3.13)$$

The resulting system of differential equations is often solved numerically, and in the present work this is done using Python and SciPy⁶⁷. Before integration, the initial conditions are specified, which is important as different initial conditions can lead to different steady states. The steady state is reached when all coverages are constant in time. A common situation is that the rate constants vary by several order of magnitudes, which makes the equations stiff. Therefore, an integration method that handles stiff problems must be chosen, and in the present work the Backward Differentiation Formula⁶⁸ method was found to be most effective.

3.3 Kinetic Monte Carlo

Kinetic Monte Carlo⁶⁹ (KMC) is a stochastic method to solve the chemical master equation (3.1). KMC must be applied in situations when the adsorbate distribution is not random or the system is finite-sized. A nanoparticles is an example of a finite system with specific adsorbate patterns. In KMC, the system starts in a specific state, and evolves in time to different states governed by random number generation. KMC solves the master equation by simulating the transitions between states as a function of time. This is done by performing a large number of reaction events and their time of observation.

The KMC method can be implemented using various algorithms, for which two popular choices are the Variable Step Size Method (VSSM) and the First-reaction method (FRM)⁶³ (Chap. 3). VSSM and FRM are two implementations of the same method, which is also known as the n-fold way⁷⁰. In the present work, the shortest computational time is obtained using the FRM algorithm. Before performing a simulation, the types of possible reaction events are defined. When this is done, FRM can be performed by a series of steps, which are summarized in Figure 3.1.

Step 1: The simulation is initialized by setting time $t = 0$, defining when the simulation should end (t_{end}), choosing the reaction conditions, and initializing the site occupations. Here an event-list is initialized to keep track of possible reaction events, their time of occurrence, and the site where they proceed. The event-list is updated at each simulation step.

Step 2: For all possible events, the times of occurrence are calculated, and the event-list is populated. The time of occurrence $t_{\beta\alpha}$ for taking the system from state α to state β is calculated according to⁶³ (p. 53)

$$t_{\beta\alpha} = t - \frac{1}{W_{\beta\alpha}} \ln u \quad (3.14)$$

Where t is the current simulation time, $W_{\beta\alpha}$ is the rate constant of the event, and u is a random uniform deviate on the interval $]0, 1]$.

Step 3: Determines whether the simulation has ended by checking if $t \geq t_{\text{end}}$.

Step 4: Performs the chronologically next reaction in the event-list. If the next reaction is impossible, it is discarded and the next possible event is performed.

Step 5: The event-list is updated by adding new events made possible by the last simulation step. This only done in a neighborhood around the site where the last event happened, since avoiding updating globally saves a significant amount of computational resources for large systems.

Step 6: Defines the end of the simulation, where quantities of interest are saved. To lower the memory consumption, saving data and cleaning different lists should also be done during the simulation.

1. Initialize Simulation : Set simulation time ($t = 0$), simulation end-time t_{end} , temperature, pressure, and initial site-occupations.
2. Populate event-list and generate occurrence times $t_{\beta\alpha}$.
3. Is $t \geq t_{\text{end}}$? If yes skip to 6
4. Perform next possible event in queue, and set t to $t_{\beta\alpha}$ of the chosen event.
5. Update list of possible events. Jump to 3
6. Finalize simulation: Save results.

Figure 3.1: First Reaction Method Algorithm.

The sites and their mutual connectivity must be represented somehow in kinetic Monte Carlo simulations. In Paper III, neighbor lists are used to define the connection between sites. The neighbor lists for all sites constitute a global connectivity pattern. Alternatively, a lattice-based algorithm can be implemented, where the connected sites are adjacent on a lattice. The implemented neighbor-list approach has an advantage over a lattice-based approach, as incommensurate lattices and dynamical catalyst changes can be accounted for in a simpler manner.

The time-step in the simulations is governed by the rate of the fastest reactions since these events are executed with the highest probability. Figure 3.2 (left) shows time as a function of simulation step during a short Monte Carlo simulation. The time increment is small in the beginning of the simulation, and becomes larger as the simulation proceeds, which is owing to decreasing fastest rates. Figure 3.2 (right) shows a histogram over the time step. The shortest time-steps are mostly originating from the beginning of the simulation, where the reaction is far from equilibrium. The histogram resembles an exponential distribution, which is reasonable as the events essentially are Poisson processes.

A considerable challenge in KMC for chemical reactions is that the fastest reactions

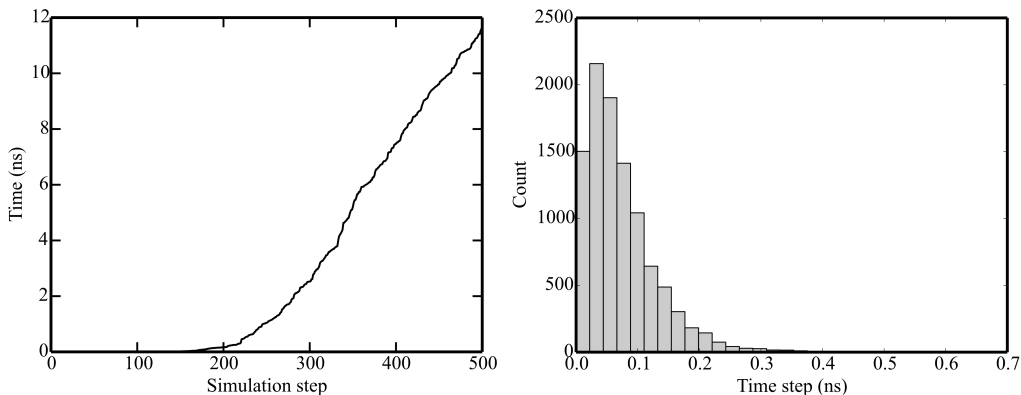


Figure 3.2: Time in kinetic Monte Carlo simulations of CO oxidation on a 5.2 nm Pt nanoparticle. Left: Time as a function of simulation step. Right: A histogram over the time step. Reaction conditions: 600 K, 20 mbar CO, and 10 mbar O₂. The CO diffusion barrier is increased by 0.5 eV.

determine the time-step. For example, diffusion events can be several orders of magnitudes faster than chemical reactions, which can make KMC simulations computationally unfeasible. To overcome this problem, one can raise the barriers of the fast events. However, this must be done with care as the fast events need to remain equilibrated. This simple method has previously been justified theoretically⁶³ (pp. 162-163). A sophisticated solution is to identify events that are in equilibrium during the simulation and increase these rate constants during the simulation⁷¹⁻⁷⁴. This can be useful when there are many possible reactions and no prior knowledge of the reactions is available.

KMC enables investigations of more realistic systems than the MFA since it does not assume complete randomness, nor an infinite number of sites. This also implies that small nanoparticles are possible to simulate. Disadvantages of KMC simulations are that the results are more complex to analyze, and that the computational cost is significantly higher than in the MFA.

3.4 Analyzing Reaction Kinetics

Microkinetic models give access to various information, which can be compared with experimental measurements. This section discusses the information that is obtained from a microkinetic simulation, and how to analyze the results in relation to experiments.

3.4.1 Reaction Mechanisms

One advantage of doing a microkinetic analysis is that it provides information about the most important reaction mechanism; provided that the relevant reaction pathways are included in the simulations. The active mechanisms are found using the net-rates, which

can be written in a mean-field picture as:

$$W_i = k_i^+ \prod_l \theta_l - k_i^- \prod_m \theta_m. \quad (3.15)$$

Where l is the set of reactant species for the elementary reaction i , and m is the set of products. In kinetic Monte Carlo, one can simply observe which reactions that are executed most frequently. The dominant reaction mechanism will be the set of reactions with the highest net-rates that complete a catalytic cycle.

3.4.2 Turnover Frequencies and Coverages

The Turnover Frequency (TOF) is a measure of the number of products formed per active site and time-unit. In a microkinetic model, the TOF is simply the net rate of product formation. Quantitative comparison between a simulated TOF and an experimental result is complicated, since there are many uncertainties and approximations involved in the modeling. Hence, it is common that the simulated TOF deviates with a few orders of magnitudes from experiments. However, the trends and variations across various reaction conditions often resemble experimental behavior.

The coverages are a simple measure to analyze the reaction, and the most abundant species can be compared to spectroscopic experiments that show the adsorbates present on the surface. Furthermore, knowing the most abundant species can assist in improving the kinetic model, for example by improving adsorbate-adsorbate interactions or entropies for the most abundant species.

3.4.3 Reaction Orders and Apparent Activation Energies

The reaction order in a given pressure and the apparent activation energy are two macroscopic quantities that can be obtained from a microkinetic model and compared to experimental values.

The reaction orders are phenomenological quantities that are defined assuming a power-law in the catalytic rate² (pp. 26-27):

$$r = K p_x^{n_x}, \quad (3.16)$$

where K is a constant with respect to pressure, p_x is the partial pressure in species x , and n_x is the reaction order in species x . To obtain n_x from simulations, the TOF is fitted to this power-law.

The apparent activation energy E_{app} is obtained by assuming an Arrhenius relation in the turnover frequency² (pp. 36-37):

$$r = A \exp\left(\frac{-E_{\text{app}}}{k_B T}\right) \prod_x p_x^{n_x}, \quad (3.17)$$

where A is a the pre-exponential factor, x is a gas-species, p_x is the pressure, and n_x is the reaction order. In practice, E_{app} is calculated numerically by evaluating the derivative of r versus $1/T$, over a narrow temperature range.

Direct comparison with experimental values is not always possible since the structure in experiments is less well-defined than in theoretical models. For the methane oxidation reaction in Paper I, the reaction orders agree well with experiments^{75;76}. However, the apparent activation energy did not agree well with experimental values⁷⁵⁻⁷⁷. This is likely due to surface-oxide formation during the experiments, which was not included in the model. In this manner, the discrepancies between experiments and a validated microkinetic model can provide important insights about the catalyst state during experiments.

3.4.4 Degree of Rate Control

The degree of rate control^{78;79} of an elementary step (χ_i) can be thought of as the sensitivity of the catalytic rate r to the individual rate constants. χ_i is defined by:

$$\chi_i = \frac{k_i^f}{r} \left(\frac{\partial r}{\partial k_i^f} \right)_{K_i}, \quad (3.18)$$

where k_i^f is the forward rate constant of step i , and the derivative is taken with a fixed equilibrium constant K_i . Thus, χ provides information on the slow steps that limit the catalytic rate. In practice, the derivative is evaluated with finite differences by increasing the rate constant of the step a small percentage, e.g. 1%. χ is important in microkinetic modeling as it determines which reaction steps that are affecting the rate, and χ can therefore provide useful information for catalyst design. Moreover, it is important to model these steps with a good accuracy.

Paper IV connects the microscopic kinetics to the reaction orders and apparent activation energies using the degree of rate control. In this way, these two macroscopic quantities are linked to the atomistic picture. The reaction orders are shown to have a simple relation with χ :

$$n_x = \sum_i \chi_i \frac{\partial \ln W_i}{\partial \ln p_x}. \quad (3.19)$$

The reaction order is a weighted sum over the individual rates W_i , derived with respect to the pressure of interest. The reaction order in the presence of a catalyst has previously been described as a phenomenological quantity⁸⁰, however, the connection between reaction orders and the elementary reactions are shown in (3.19).

The relation between χ and the apparent activation energy takes the form

$$E_{\text{app}} = \sum_{i \in \text{vib}} \chi_i \left(E_i + k_{\text{B}}T + k_{\text{B}}T^2 \frac{\partial S_i}{\partial T} \right) + \sum_{j \in \text{trans}} \chi_j \left(E_j - \frac{k_{\text{B}}T}{2} + k_{\text{B}}T^2 \frac{\partial P_j}{\partial T} \right) \quad (3.20)$$

$$- k_{\text{B}}T^2 \sum_x \frac{\partial n_x}{\partial T} \ln p_x$$

Where E_i is the energy barrier of elementary step i , S_i is the entropic barrier, and P_j is the sticking coefficient related to step j . n_x is the reaction order in species x , and p_x is the partial pressure. The first sum runs over the steps that have a vibration as the reaction coordinate, and the second sum is over reactions with a translational reaction

coordinate. The third sum accounts for the pressure dependence of the total rate. It is interesting to note that the zeroth order contribution in temperature is the largest and arises from the elementary energy barriers. The first-order temperature terms arise from a lost degree of freedom in the reaction coordinate, and the second order terms stem from entropic losses and pressure dependencies.

The derived expressions provide a microscopic understanding of the reaction orders and apparent activation energies. Furthermore, the expressions might be used to evaluate proposed rate-determining steps and reaction mechanisms, for example by combining DFT calculations and experimental measurements.

3.5 Summary

The present chapter has discussed how the chemical master equation describes the reaction kinetics. The mean-field approximation was derived as an approximate solution to the master equation, and Kinetic Monte Carlo was presented as a stochastic method to solve the master equation. Finally, analysis of results obtained from microkinetic models was discussed with focus on comparing with experiments.

Chapter 4

Kinetic Models for Methane and CO Oxidation

4.1 Constructing a Kinetic Model

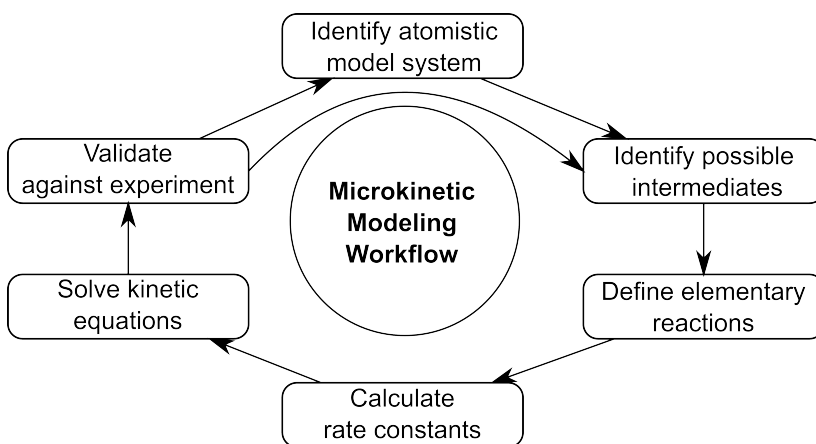
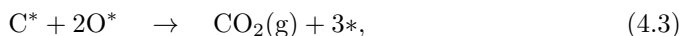


Figure 4.1: Illustration of workflow for constructing a first-principles microkinetic model.

The microkinetic models in this thesis are constructed using a workflow illustrated in Figure 4.1. Formulation and refinement of a model is an iterative procedure, where the cycle in Figure 4.1 is completed multiple times before settling on a final version of the kinetic model. The workflow begins with identifying an atomistic model system of the catalyst. This is often a crucial and difficult step as technical catalysts are complex systems, which are ill-defined with respect to structure and composition. The next step is to identify possible intermediates. These intermediates are connected by multiple elementary reaction steps, which together constitute the catalytic cycle. Taking complete methane oxidation to CO_2 over Pd surfaces as an example, the atomistic model system can be Pd(100) or Pd(111). Plausible intermediates are hydrocarbons, oxygen, carbon, and CO. Thereby, a starting point for a possible reaction mechanism could be:



These steps are not elementary, and should be reformulated as elementary steps, possibly by including alternative pathways. After the intermediates and elementary reactions have been identified, rate constants are calculated for the considered elementary steps and the kinetic equations are solved. Thereafter, the computational results are compared to experimental data by simulating measurable quantities, such as turnover frequencies, reaction orders, and apparent activation energies. The cycle is repeated until the model has the desired level of detail and agrees with experimental data. A validated microkinetic model opens up the possibility to use the simulations for predictions beyond the experimentally investigated conditions.

4.2 Complete Methane Oxidation over Pd(100) and Pd(111)

In Paper I, the mean-field approximation is applied to model complete methane oxidation over Pd(100) and Pd(111), which is a complex reaction with several possible intermediates and mechanisms. The reaction is important to understand as methane is a potent greenhouse gas, which has a larger global warming potential than CO₂^{81;82}. Moreover, complete methane oxidation to CO₂ is becoming an increasingly important reaction for the automotive industry as the global natural-gas vehicle fleet is growing⁸³. The overall reaction is:



Pt and Pd are known to be active catalysts, where Pt is superior in net reducing conditions and Pd is advantageous in net oxidizing environments⁸⁴. Pd oxidizes readily at most reaction conditions^{82;85-87} and the high activity has previously been attributed to the oxidized phase^{85;88}, whereas other reports assigned the high activity to the metallic state⁸⁹⁻⁹¹. The metallic phase is difficult to stabilize during experiments, which makes a first-principles microkinetic model a useful tool. Furthermore, a microkinetic model reveals active reaction mechanisms and kinetic bottlenecks that can help improve the reaction.

The kinetic model developed in this work extends a previous model of the reaction over metallic Pd³⁶, by taking into account a large number of reaction barriers and multiple reaction mechanisms. One purpose of constructing a refined model is to compare with a detailed model of the reaction over PdO(101)³⁵. By comparing models of metallic Pd and PdO, differences are revealed between the two phases, which is important in order to determine the most active phase.

The simulations are performed in slight oxygen excess with pressures of 0.61 mbar methane and 3.06 mbar oxygen. The model includes six gas-phase species, 16 adsorbed species, and 32 elementary reactions, which enables multiple reaction pathways. The included gas-phase species are: CH₄, O₂, CO₂, H₂O, CO, and H₂. Included adsorbates are: CH₃, CH₂, CH, C, H, O₂, O, CO, OH, H₂O, CH₂OH, CH₂O, CHO, COH, OCOH, and CHOH. The reaction is found to proceed via different mechanisms depending on the reaction conditions. At high temperatures, methane is dehydrogenated on the surface one hydrogen at a time to C + 4H. Thereafter, C is oxidized to CO and further to CO₂ by O. Simultaneously, H is oxidized to H₂O, mainly via OH + OH → H₂O + O. At lower temperatures, instead C is oxidized by OH, and the mechanism involves steps such as C + OH → COH and COH + O → OCOH.

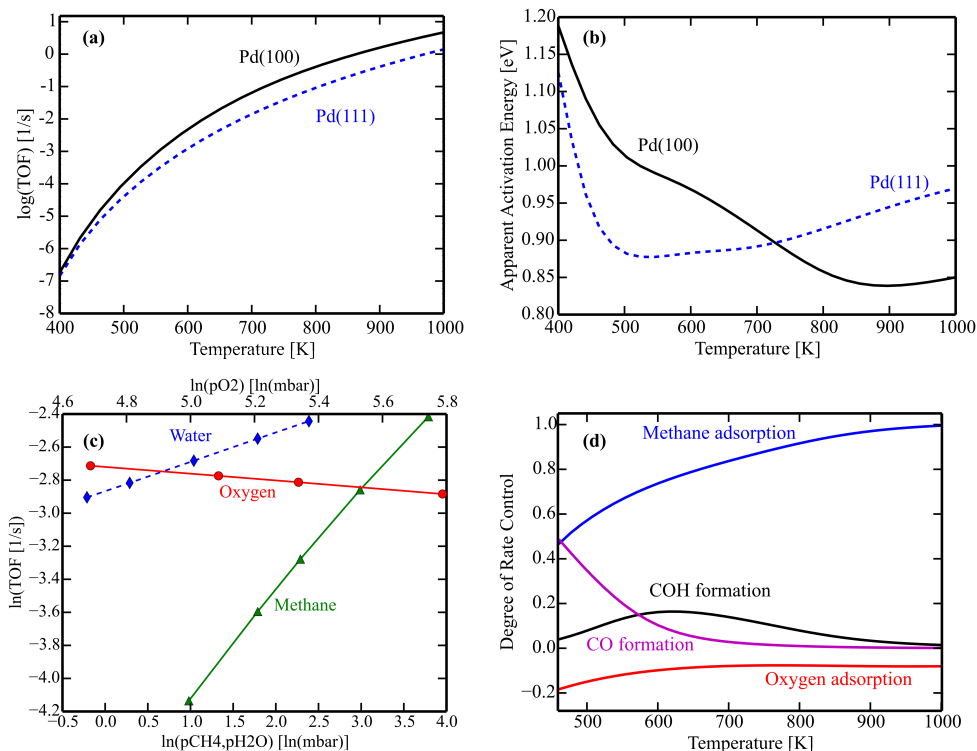


Figure 4.2: Simulated kinetics of methane oxidation at 0.61 mbar methane and 3.06 mbar oxygen. (a) Turnover frequencies versus temperature. (b) Apparent activation energies versus temperature. (c) Turnover frequency versus pressures on Pd(100) at 598 K. (d) Degree of rate control versus temperature on Pd(100).

The coverages and TOFs are central quantities for understanding the kinetics. The simulations predict that the most abundant adsorbates on the surfaces are O, C and CO. O is present at all investigated temperatures on both Pd(100) and Pd(111), whereas C and CO only are present at low temperatures. The simulated TOFs are shown in Figure 4.2 (a). The TOFs vary seven orders of magnitudes when increasing the temperature from 400 to 1000 K, and the Pd(100) surface is found to be more active than Pd(111) at all investigated conditions.

The apparent activation energy (E_{app}) reflects the Gibbs free energy barriers of the rate controlling steps, as was derived in Paper IV. The simulated E_{app} is shown in Figure 4.2 (b). E_{app} varies between 1.2 and 0.85 eV for Pd(100) in the temperature range 400-1000 K. The variation is due to changing reaction mechanisms and rate-controlling steps. An analytical expression is derived for E_{app} in the limit of high temperatures, which shows that E_{app} is determined by the methane adsorption barrier and the oxygen

adsorption/desorption equilibrium as:

$$E_{\text{app}} \approx E_{\text{CH}_4}^f - \frac{\sqrt{p_{\text{O}_2} K_{\text{O}_2}} \Delta E_{\text{O}_2}}{1 + \sqrt{p_{\text{O}_2} K_{\text{O}_2}}}, \quad (4.5)$$

where $E_{\text{CH}_4}^f$ is the energy barrier for methane dissociative adsorption, p_{O_2} is the oxygen pressure, ΔE_{O_2} is the dissociative adsorption energy of O_2 , and K_{O_2} is the equilibrium constant for oxygen adsorption.

The reaction order reflects how the TOF responds to a change in pressure. Figure 4.2 (c) shows the logarithm of the TOF as a function of methane, oxygen, and water pressure on Pd(100). The results for Pd(111) are similar. The analysis shows that a higher methane pressure increases the TOF. Conversely, oxygen is inhibiting the rate by blocking sites for methane dissociation, and water can promote the reaction by increasing the rate of $\text{C} + \text{OH} \rightarrow \text{COH}$, which is a rate-controlling step.

The degree of rate control analysis is a way to explain the kinetics in a compact manner. The simulated degree of rate controls are shown in Figure 4.2 (d) for the main steps. The main rate-controlling steps at low temperatures are $\text{C} + \text{OH} \rightarrow \text{COH}$ and $\text{C} + \text{O} \rightarrow \text{CO}$. At higher temperatures, dissociative methane adsorption eventually becomes the rate-determining step. Oxygen adsorption is slightly inhibiting over the entire temperature range. These observations are reflected in the coverages as the most abundant species are connected to the rate-controlling steps. The presence of C on the surface suggests that oxidizing C has a finite rate-control, in agreement with the analysis. The reaction orders are also explained by the degree of rate control, as is derived in Paper IV. The reaction order in methane follows the degree of rate control for methane dissociation closely (Paper I and Paper IV). The slightly negative oxygen order shows that oxygen adsorption is an inhibition step, and thus has a negative rate control. The positive order in the water pressure is readily understood by noting that increasing the OH concentration speeds up a rate-controlling step: $\text{C} + \text{OH} \rightarrow \text{COH}$. The apparent activation energy is also connected to the degree of rate control (Paper IV). The high-temperature analytical expression for the apparent activation energy (4.5), reflects that methane adsorption is the most rate-controlling step, and oxygen adsorption is a slightly inhibiting step.

The model in Paper I for metallic Pd can be compared with methane oxidation over PdO(101), which has been modeled in detail previously³⁵. The reaction orders in the methane pressure are high and positive for both PdO^{35;75-77} and metallic Pd surfaces. However, the PdO catalyst has qualitatively different reaction orders in the water and oxygen pressures. Water is known to be poisoning the PdO catalyst^{35;75-77;92} due to site-blocking effects, whereas water can promote the reaction on metallic Pd. Oxygen can promote the reaction on PdO at some conditions^{35;76;77}, whereas it inhibits the reaction on metallic Pd. These clear qualitative differences between Pd and PdO can aid characterization of the active phase using only the reaction kinetics.

The aforementioned results apply to extended surfaces, however, technical catalysts are nanostructured materials. The presence of low-coordinated sites on nanoparticles will likely promote this reaction⁸ as methane adsorption is the rate-determining step. Thus, nanoparticles are expected to be more active for the reaction than extended surfaces, given that other effects are not hindering the rate. The benefit of having a multitude of sites in complete methane oxidation on nanoparticles remains to be investigated.

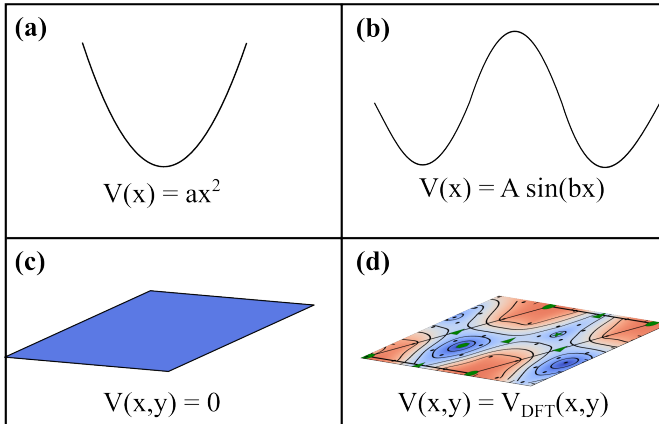


Figure 4.3: Schematic illustration of the potential energy landscape for translation in (a) the Harmonic Approximation, (b) Hindered Translator, (c) Free Translator, and (d) CPES.

4.3 Entropic Effects in CO Oxidation on Pt(111)

In Paper II, different models for adsorbate entropy are investigated. Previous first-principles microkinetic models have typically described adsorbate-entropies in the Harmonic Approximation^{31;66;93}. Alternatively, weakly bound adsorbates have been treated as losing one or all translational degrees of freedom upon adsorption^{30;94–96}. Therefore, detailed investigations of entropy in the context of microkinetic modeling is beneficial. CO oxidation over Pt(111) is used as an archetype reaction. This reaction is very well-studied^{30;97–105}, and this enables a detailed comparison to experiments. The reaction is modeled in the mean-field approximation using a Langmuir-Hinselwood mechanism^{30;97;100–102;105;106}:



The entropies of CO and O are found to be qualitatively different. CO translates on a flat potential energy surface with low diffusion barriers, which results in a high entropy. O instead clearly prefers fcc binding and has high diffusion barriers, which results in a low entropy. Typically, a mean-field model includes only a generic and coarse-grained site, and it is blind to the detailed nature of the site. The coarse-grained site could entail fcc, hcp, ontop, and bridge sites. When the adsorption energies on these sites are similar, the translational entropy can be high and should be modeled accordingly.

Four different models for adsorbate entropy are evaluated: The Harmonic Approximation (HA), the Hindered Translator (HT), the Free Translator (FT), and the method of Complete Potential Energy Sampling (CPES). The four models are described in detail in section 2.6. The four methods differ in how the potential energy landscape for translation

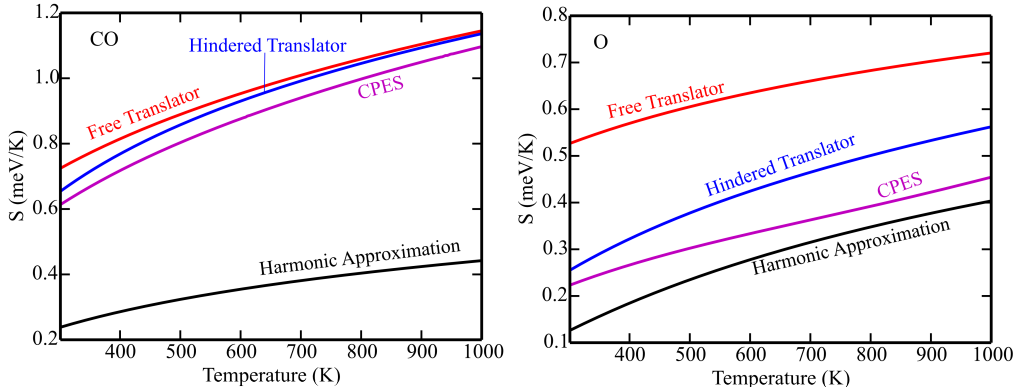


Figure 4.4: Calculated adsorbate entropy versus temperature of CO (left) and O (right) for one adsorbate in one Pt(111) fcc unit-cell.

is modeled. Figure 4.3 shows a schematic illustration of the potentials in the four models. The Harmonic Approximation has a quadratic potential along the surface, the Hindered Translator is sinusoidal, the Free Translator is unbound, and the CPES method uses the potential energy landscape calculated by DFT.

The entropies predicted by the four approximations are given in Figure 4.4 for one adsorbate in a single unit-cell. For both CO and O, the Harmonic Approximation predicts the lowest entropies, as it fixates the adsorbate to one site¹. The Free Translator predicts the highest entropies since it assumes barrierless adsorbate-diffusion. The Hindered Translator and CPES predict entropies in between these two extremes. The Harmonic Approximation gives an entropy for CO that is 0.4 meV/K lower than CPES. At 500 K, this corresponds to a difference in adsorption energy of 0.2 eV, which can be considered a significant difference.

The choice of entropy model affects the kinetics significantly, and the predicted TOFs vary between the four models. The largest TOF is predicted in the Harmonic Approximation, where the adsorbate entropy is lowest, and the lowest TOF is obtained using the Free Translator that is an upper bound to the translational entropy. The coverages are also affected by the entropy. The lowest coverages are obtained in the Harmonic Approximation, whereas the highest coverages are found using the Free Translator. Additionally, entropy affects the light-off temperatures, i.e. the temperature for where the turnover frequency reaches half maximum. Figure 4.5 shows a comparison between light-off temperatures obtained by the developed kinetic model and various experiments^{97;99;102;105}. The Harmonic Approximation and Free Translator under and overestimate the light-off temperature, respectively. The light-off temperatures predicted by the Hindered Translator and CPES are in good agreement with the experimental references over the entire pressure-range. Hence, modeling the entropy in detail moves the results significantly closer to experimentally obtained values. The effect of entropy on the kinetics is readily understood by noting that a high entropy implies a stronger adsorbate-surface bond. This

¹For example either fcc, hcp, bridge, or ontop

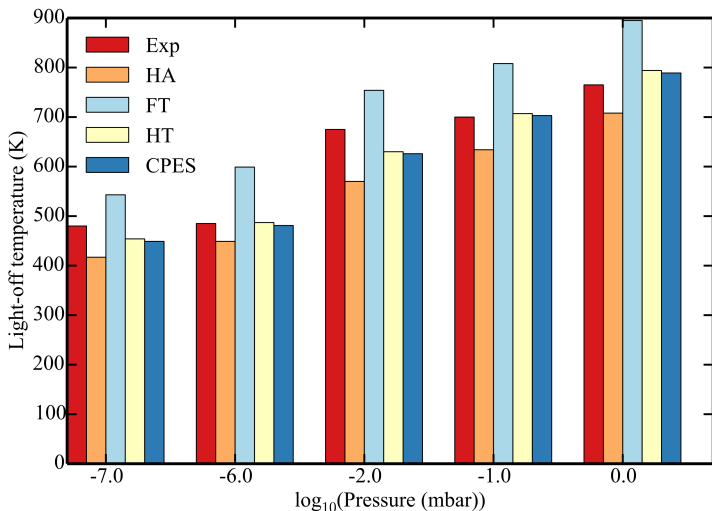


Figure 4.5: Simulated and experimental (Exp) light-off temperatures as a function of pressure. The experimental references are: Campbell et al.⁹⁷ (10^{-7} mbar), Vogel et al.¹⁰² (10^{-6} mbar), Nakao et al.⁹⁹ (10^{-2} mbar), and Calderón et al.¹⁰⁵ (10^{-1} - 10^0 mbar).

effect is enhanced with increasing temperatures as $\Delta G = \Delta E - T\Delta S$.

The overall conclusions of this study are that the treatment of adsorbate entropy affects the results of the kinetic simulations, and mobile molecules should not be modeled in the Harmonic Approximation.

4.4 Catalysis on Nanoparticles

Commercial catalysts often consist of metal nanoparticles, which implies that reactions should be modeled using finite-sized systems. Therefore, to understand catalytic behavior it is important to model nanoparticles. Nanoparticles are different from extended surfaces as nanoparticles have different sites with various reactivities. As a consequence, the kinetics is complex, and the mean-field approximation breaks down. Instead kinetic Monte Carlo simulations should be applied.

When modeling nanoparticles, a large number of energies is required to represent the reaction energy landscapes. Moreover, the reaction energies on extended surfaces and nanoparticles can differ significantly^{8;9;11;107}. Kinetic Monte Carlo models have previously been formulated for nanoparticles using simplified energy landscapes^{38;40} and schematic reactions^{49;50}. However, few studies have simulated a specific reaction using a detailed reaction energy landscape.

In paper III, CO oxidation is modeled on Pt nanoparticles by developing a KMC algorithm. The paper outlines a method to simulate nanoparticles by approximating the reaction energy landscape. The energy landscape is approximated using generalized coordination numbers, which lowers the computational cost significantly. Recently, the

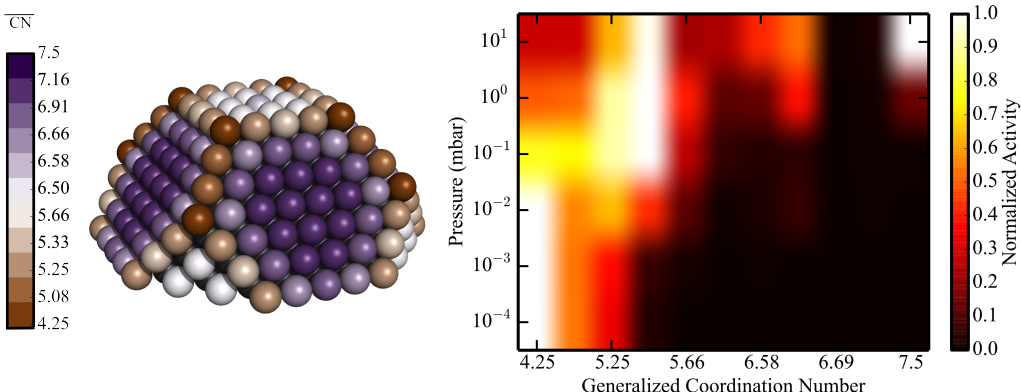


Figure 4.6: Left: Generalized coordination numbers of ontop sites on a 2.8 nm nanoparticle. Right: Activity of CO oxidation versus pressure and generalized coordination number on a 2.8 nm Pt nanoparticle. The temperature is 850 K, and the pressure ratio $p_{\text{CO}}/p_{\text{O}_2} = 2$.

generalized coordination number \overline{CN} was shown to be a good descriptor for adsorption energies on nanoparticles and surfaces^{19–21}. \overline{CN} is an extension of the conventional coordination number, which accounts for the coordination numbers of the nearest neighbors as:

$$\overline{CN} = \sum_{i \in \{NN\}} \frac{CN_i}{CN_{\text{max}}}, \quad (4.7)$$

where the sum runs over the nearest neighbors to the site in question, CN_i is the conventional coordination number of the nearest neighbor i , and CN_{max} is the maximally possible coordination number of neighbors in the bulk. In a fcc crystal, the ontop site has $CN_{\text{max}} = 12$, a bridge has $CN_{\text{max}} = 18$, a three-fold hollow has $CN_{\text{max}} = 22$, and for a four-fold hollow site $CN_{\text{max}} = 26$. Figure 4.6 (left) shows \overline{CN} for ontop sites on a nanoparticle, where each color corresponds to one \overline{CN} and hence one adsorption energy. Furthermore, in Paper III the reaction energy barriers are obtained by a Brønsted-Evans-Polanyi (BEP) relation, which relates the adsorption energies to the transition state. Using BEP relations, coverage dependencies in the reaction barriers are accounted for automatically. In this manner, \overline{CN} fully describes the reaction energy landscape with limited computational effort.

CO oxidation over Pt is taken as a model reaction to study the effects of modeling nanoparticles on the reaction kinetics. By comparing simulations on nanoparticles with the extended Pt(111) surface, conclusions can be drawn concerning the materials gap. The model predicts that nanoparticles have a higher TOF than the Pt(111) surface. One reason is that the rate is not limited by adsorption as opposed to Pt(111). This is owing to the low-coordinated sites on the nanoparticle that can contribute to the reaction at high temperatures. Thus, the active site varies with reaction conditions, and as a consequence the TOF scales with particle size. The most active sites at 850 K are illustrated in Figure 4.6 (right). Here, the catalytic activity is divided by the highest activity at each pressure,

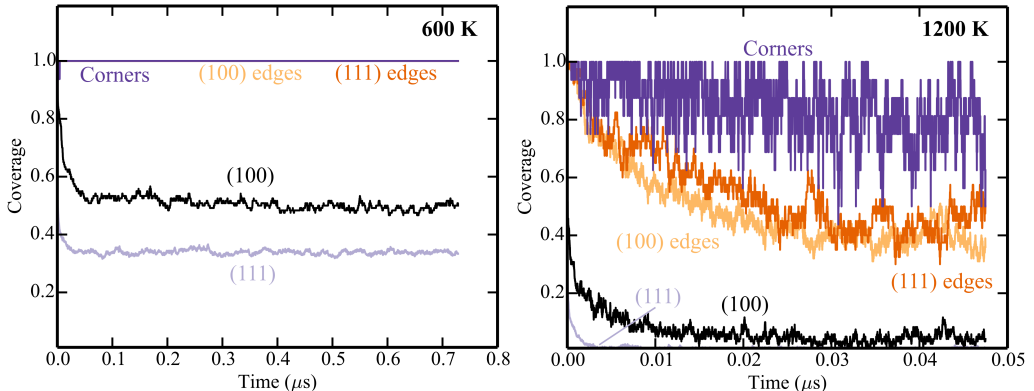


Figure 4.7: Simulated CO coverage in CO oxidation over a 5.2 nm Pt nanoparticle. Left: Temperature of 600 K. Right: Temperature of 1200 K. Pressures: 20 mbar CO and 10 mbar O_2 . The CO diffusion barrier is increased by 0.5 eV.

and it is normalized to the number of sites with the given \overline{CN} . At low pressures, edges and corners ($\overline{CN} < 5.66$) are active, which implies that the TOF declines with increasing particle size. At high pressures, the edges and facets ($\overline{CN} > 4.25$) are most active, and the TOF grows with particle size. Similarly, temperature affects the most active site. At high temperatures, the corners and edges are most active, whereas low temperatures make the edges and facets most active. These results demonstrate that nanoparticles cannot be represented fully by extended surfaces. Furthermore, the results clearly indicate that the mean-field approximation breaks down on nanoparticles as a mean-field model cannot account for the site-distribution, which is important to capture the kinetics.

Paper III shows the average kinetic behavior, which is most relevant in studying catalysts that operate over long time scales. However, the time evolution of a simulation is also instructive to consider. Figure 4.7 shows the CO coverage on a nanoparticle during a short simulation. At 600 K (left), the facets contain free sites, whereas the edges and corners are completely filled. At 1200 K (right), the coverages are lower on the edges, whereas the corners and facets are empty. One interesting observation is that there are large fluctuations in the coverages, which are most pronounced for the low-coordinated sites as they are less abundant. The magnitude of the fluctuations increases with temperature and becomes considerable for smaller systems. A mean-field model assumes that such fluctuations can be neglected, which is clearly not valid on nanoparticles.

To understand the relation between structure and catalytic activity, it is instructive to sequentially increase the complexity of the model system. An example is to start by understanding extended surfaces, then stepped surfaces, nanoparticles, supported nanoparticles, etc. However, the level of detail can reach a point where the results are too complex and unclear to comprehend. Moreover, as DFT does not yield chemical accuracy, at some point the results might be inaccurate. The present work has taken a step from extended surfaces to truncated octahedral nanoparticles by using scaling relations derived from DFT. This approach might seem rough at a first glance. However, calculating all

energies explicitly is less meaningful as the octahedral nanoparticle is to be considered a model system, and due to the limited accuracy of DFT.

From the developed model, structure-activity relationships can be investigated, which can be useful in catalyst design. The results indicate that a search for one single active site might be a too simplistic approach on nanoparticles as various sites likely collaborate to enable the reaction to follow a path of least resistance. With the developed method, kinetic modeling of actual reactions can be performed routinely with limited computational effort, and doing this will be a significant step towards bridging the materials gap.

Chapter 5

Conclusion & Outlook

The presented work has aimed to investigate and develop the methodology for first-principles microkinetic modeling of catalytic reactions. This was realized in a series of papers that addressed various topics.

Complete methane oxidation over extended palladium surfaces was modeled in detail, which revealed the rate-controlling steps and detailed reaction mechanisms. The mechanisms on metallic Pd were found to be fundamentally different from those on PdO, which leads to interesting variations between the kinetics of the two phases.

The effect of adsorbate entropy was studied by developing a mean-field model of CO oxidation over Pt(111). This revealed how adsorbate entropy affects the kinetic behavior. Furthermore, Complete Potential Energy Sampling was developed to have a systematic method for estimating entropies of adsorbates.

Additionally, this thesis has addressed the materials gap between extended surfaces and nanoparticles in heterogeneous catalysis, where a microkinetic model was developed for CO oxidation on Pt nanoparticles and Pt(111). The model was based on scaling relations in the generalized coordination numbers, and the kinetics was simulated by developing a kinetic Monte Carlo algorithm. Generalized coordination numbers provide a computationally cheap procedure to account for the reaction energy landscape on nanoparticles.

Finally, as a method to link theoretical simulations and experimental studies, the degree of rate control was shown to be connected to reaction orders and apparent activation energies. In this way, the present work has provided a microscopic understanding of these two phenomenological quantities.

Compared to previous literature, this thesis has developed the methodology for modeling reactions in heterogeneous catalysis. Previously, methane oxidation over Pd surfaces has been modeled with a limited number of mechanisms. By inclusion of several alternative reactions, a more reliable reaction mechanism was obtained in the present work. Previously, reactions have mostly been simulated on extended surfaces. This thesis has developed a scheme to facilitate simulations on nanoparticles by using the generalized coordination numbers. The entropy of adsorbates has previously been of secondary concern in microkinetic models. The present work has investigated the importance of entropy in kinetic modeling, and it has developed the CPES method to calculate the entropy from first principles. Reaction orders and apparent activation energies have previously not been connected to the microscale. This work has enabled such an understanding by coupling the reaction orders and apparent activation energies to the degree of rate control.

To further improve microkinetic modeling, there are several interesting aspects that can be studied to extend this thesis. For example, the method of modeling adsorbate-adsorbate interactions can be studied in greater detail, both for adsorption energies and entropies.

The developed kinetic Monte Carlo method can be applied for improved catalyst screening studies, since it explicitly simulates nanoparticles. One limitation of the present work is that it treats the catalyst as a static entity without including morphological changes. Such dynamical changes can possibly be simulated by combining the developed Monte Carlo algorithm with molecular dynamics. Furthermore, an oxide-support can be included in the simulations to study possible spill-over phenomena.

Future catalyst design can benefit from understanding the active reaction mechanisms, thermodynamics, and kinetic behavior in catalysis. In the future, when the computational power has matured sufficiently, catalyst design can possibly be realized using computational methods to a larger degree. An important part of this is the development of methodologies for accurate microkinetic modeling.

As Richard Feynman envisioned it in his talk¹ almost 60 years ago, presently we have a much greater range of possibilities for manipulating and designing nanoscaled systems. When designing nanoscale technology, it is beneficial to understand the quantum mechanical behavior of systems of atoms. This thesis has taken steps towards understanding the detailed behavior of atomic systems.

Acknowledgments

The research presented herein was carried out at the Division of Chemical Physics and Competence Centre for Catalysis at Chalmers University of Technology, Göteborg, Sweden in the period August 2015 to July 2017.

The research is funded by Chalmers Area of Advance Nanoscience and Nanotechnology, the Competence Centre for Catalysis, and the Swedish Research Council. Computational time has been granted by SNIC at C3SE (Göteborg) and PDC (Stockholm).

The Competence Centre for Catalysis is hosted by Chalmers University of Technology and financially supported by the Swedish Energy Agency and the member companies AB Volvo, ECAPS AB, Haldor Topsøe A/S, Scania CV AB, Volvo Car Corporation AB and Wärtsilä Finland Oy.

In addition I would like to acknowledge a non-exhaustive list of people:

My main supervisor, Henrik Grönbeck. Thank you for investing a lot of time and effort in supervising this project and for our many scientific discussions. It has been very developing to learn from your analytical skills and scientific insights.

My co-supervisor, Anders Hellman. You are acknowledged for serious as well as informal discussions about theory in practice.

All my colleagues at Chemical Physics are acknowledged. Thank you for creating a pleasant and nice working environment. I especially would like to thank Adam, Anna, Alvaro, Baochang, Chris, Lin, Matthias, Maxime, Michael, Mikael, Oskar, and Unni.

I would also like to acknowledge the members of the Competence Centre for Catalysis. In particular I would like to thank Carl-Robert, David, Emma, Johan, Peter, Ting, and Torben.

At last but not least, I want to thank my family and Dorte for making this possible by providing me with extraordinary support and patience. Without you this thesis would not have been.

Finally, thank you all for entering the same many-body wavefunction as I. This might mean more than we realize.

Bibliography

- [1] Feynman, R. P. There's Plenty of Room at the Bottom. *J. Microelectromech. Syst.*, *1* (1992), 60–66. doi: 10.1109/84.128057.
- [2] Chorkendorff, I. and Niemantsverdriet, J. W. *Concepts of Modern Catalysis and Kinetics*. WILEY-VCH Verlag GmbH & Co. KGaA, Weinheim, second, revised and enlarged edition, 2007.
- [3] Taylor, H. S. A Theory of the Catalytic Surface. *Proc. R. Soc. Lond. A*, *108* (1925), 105–111. doi: 10.1098/rspa.1925.0061.
- [4] Hohenberg, P. and Kohn, W. Inhomogeneous Electron Gas. *Phys. Rev.*, *136* (1964), B864–B871. doi: 10.1103/PhysRev.136.B864.
- [5] Kohn, W. and Sham, L. J. Self-Consistent Equations Including Exchange and Correlation Effects. *Phys. Rev.*, *140* (1965), A1133–A1138. doi: 10.1103/PhysRev.140.A1133.
- [6] Nørskov, J. K.; Abild-Pedersen, F.; Studt, F.; and Bligaard, T. Density Functional Theory in Surface Chemistry and Catalysis. *PNAS*, *108* (2011), 937–943. doi: 10.1073/pnas.1006652108.
- [7] Van Santen, R. A. and Neurock, M. Concepts in Theoretical Heterogeneous Catalytic Reactivity. *Catal. Rev. Sci. Eng.*, *37* (1995), 557–698. doi: 10.1080/01614949508006451.
- [8] Kozlov, S. M. and Neyman, K. M. Insights from Methane Decomposition on Nanostructured Palladium. *J. Catal.*, *337* (2016), 111–121. doi: 10.1016/j.jcat.2016.02.010.
- [9] Fajín, J. L. C.; Bruix, A.; Cordeiro, M. N. D. S.; Gomes, J. R. B.; and Illas, F. Density Functional Theory Model Study of Size and Structure Effects on Water Dissociation by Platinum Nanoparticles. *J. Chem. Phys.*, *137* (2012). doi: 10.1063/1.4733984.
- [10] Jennings, P. C.; Aleksandrov, H. A.; Neyman, K. M.; and Johnston, R. L. A DFT study of Oxygen Dissociation on Platinum based Nanoparticles. *Nanoscale*, *6* (2014), 1153–1165. doi: 10.1039/c3nr04750d.
- [11] Viñes, F.; Lykhach, Y.; Staudt, T.; Lorenz, M. P. A.; Papp, C.; Steinrück, H.-P.; Libuda, J.; Neyman, K. M.; and Görling, A. Methane Activation by Platinum: Critical Role of Edge and Corner Sites of Metal Nanoparticles. *Chem. Eur. J.*, *16* (2010), 6530–6539. doi: 10.1002/chem.201000296.
- [12] Lopez-Acevedo, O.; Kacprzak, K. A.; Akola, J.; and Häkkinen, H. Quantum Size Effects in Ambient CO oxidation Catalysed by Ligand-Protected Gold Clusters. *Nat. Chem.*, *2* (2010), 329–334. doi: 10.1038/NCHEM.589.

- [13] Zheng, Z. and Greeley, J. Theoretical study of CO Adsorption on Au Catalysts under Environmental Catalytic Conditions. *Catal. Commun.*, 52 (2014), 78–83. doi: 10.1016/j.catcom.2014.03.016.
- [14] Yudanov, I. V.; Sahnoun, R.; Neyman, K. M.; Rösch, N.; Hoffmann, J.; Schauer mann, S.; Johánek, V.; Unterhalt, H.; Rupprechter, G.; Libuda, J.; and Freund, H.-J. CO Adsorption on Pd Nanoparticles: Density Functional and Vibrational Spectroscopy Studies. *J. Phys. Chem. B*, 107 (2003), 255–264. doi: 10.1021/jp022052b.
- [15] Posada-Borbón, A.; Heard, C. J.; and Grönbeck, H. Cluster Size Effects in Ethylene Hydrogenation over Palladium. *J. Phys. Chem. C*, 121 (2017), 10870–10875. doi: 10.1021/acs.jpcc.6b12072.
- [16] Kleis, J.; Greeley, J.; Romero, N. A.; Morozov, V. A.; Falsig, H.; Larsen, A. H.; Lu, J.; Mortensen, J. J.; Dulak, M.; Thygesen, K. S.; Nørskov, J. K.; and Jacobsen, K. W. Finite Size Effects in Chemical Bonding: From Small Clusters to Solids. *Catal. Lett.*, 141 (2011), 1067–1071. doi: 10.1007/s10562-011-0632-0.
- [17] Li, L.; Larsen, A. H.; Romero, N. A.; Morozov, V. A.; Glinsvad, C.; Abild-Pedersen, F.; Greeley, J.; Jacobsen, K. W.; and Nørskov, J. K. Investigation of Catalytic Finite-Size-Effects of Platinum Metal Clusters. *J. Phys. Chem. Lett.*, 4 (2013), 222–226. doi: 10.1021/jz3018286.
- [18] Hammer, B. and Nørskov, J. K. Why Gold is the Noblest of All the Metals. *Nature*, 376 (2002), 238–240. doi: 10.1038/376238a0.
- [19] Calle-Vallejo, F.; Martínez, J. I.; García-Lastra, J. M.; Sautet, P.; and Loffreda, D. Fast Prediction of Adsorption Properties for Platinum Nanocatalysts with Generalized Coordination Numbers. *Angew. Chem., Int. Ed.*, 53 (2014), 8316–8319. doi: 10.1002/anie.201402958.
- [20] Calle-Vallejo, F.; Loffreda, D.; Koper, M. T. M.; and Sautet, P. Introducing Structural Sensitivity into Adsorption–Energy Scaling Relations by means of Coordination Numbers. *Nat. Chem.*, 7 (2015), 403–410. doi: 10.1038/nchem.2226.
- [21] Calle-Vallejo, F.; Tymoczko, J.; Colic, V.; Vu, Q. H.; Pohl, M. D.; Morgenstern, K.; Loffreda, D.; Sautet, P.; Schuhmann, W.; and Bandarenka, A. S. Finding Optimal Surface Sites on Heterogeneous Catalysts by Counting Nearest Neighbors. *Science*, 350 (2015), 185–189. doi: 10.1126/science.aab3501.
- [22] Stoltze, P. and Nørskov, J. K. Bridging the "Pressure Gap" between Ultrahigh-Vacuum Surface Physics and High-Pressure Catalysis. *Phys. Rev. Lett.*, 55 (1985), 2502–2505. doi: 10.1103/PhysRevLett.55.2502.
- [23] Aparicio, L. M. and Dumesic, J. A. Ammonia Synthesis Kinetics: Surface Chemistry, Rate Expressions, and Kinetic Analysis. *Top. Catal.*, 1 (1994), 233–252. doi: 10.1007/BF01492278.

- [24] Aparicio, L. M.; Rossini, S. A.; Sanfilippo, D. G.; Rekoske, J. E.; Treviño, A. A.; and Dumesic, J. A. Microkinetic Analysis of Methane Dimerization Reaction. *Ind. Eng. Chem. Res.*, *30* (1991), 2114–2123. doi: 10.1021/ie00057a009.
- [25] Dahl, S.; Sehested, J.; Jacobsen, C. J. H.; Törnqvist, E.; and Chorkendorff, I. Surface Science Based Microkinetic Analysis of Ammonia Synthesis over Ruthenium Catalysts. *J. Catal.*, *192* (2000), 391–399. doi: 10.1006/jcat.2000.2857.
- [26] Dumesic, J. A. and Trevino, A. A. Kinetic Simulation of Ammonia Synthesis Catalysis. *J. Catal.*, *116* (1989), 119–129. doi: 10.1016/0021-9517(89)90080-8.
- [27] Frank, B.; Jentoft, F. C.; Soerijanto, H.; Kröhnert, J.; Schlögl, R.; and Schomäcker, R. Steam Reforming of Methanol over Copper-Containing Catalysts: Influence of Support Material on Microkinetics. *J. Catal.*, *246* (2007), 177–192. doi: 10.1016/j.jcat.2006.11.031.
- [28] Prasad, V.; Karim, A. M.; Arya, A.; and Vlachos, D. G. Assessment of Overall Rate Expressions and Multiscale, Microkinetic Model Uniqueness via Experimental Data Injection: Ammonia Decomposition on Ru/ γ -Al₂O₃ for Hydrogen Production. *Ind. Eng. Chem. Res.*, *48* (2009), 5255–5265. doi: 10.1021/ie900144x.
- [29] Stoltze, P. and Nørskov, J. K. An Interpretation of the High-Pressure Kinetics of Ammonia Synthesis Based on a Microscopic Model. *J. Catal.*, *110* (1988), 1–10. doi: 10.1016/0021-9517(88)90291-6.
- [30] Falsig, H.; Hvolbæk, B.; Kristensen, I. S.; Jiang, T.; Bligaard, T.; Christensen, C. H.; and Nørskov, J. K. Trends in the Catalytic CO Oxidation Activity of Nanoparticles. *Angew. Chem. Int. Ed.*, *47* (2008), 4835–4839. doi: 10.1002/anie.200801479.
- [31] Honkala, K.; Hellman, A.; Remediakis, I. N.; Logadottir, A.; Carlsson, A.; Dahl, S.; Christensen, C. H.; and Nørskov, J. K. Ammonia Synthesis from First-Principles Calculations. *Science*, *307* (2005), 555–558. doi: 10.1126/science.1106435.
- [32] Hansgen, D. A.; Vlachos, D. G.; and Chen, J. G. Using First Principles to Predict Bimetallic Catalysts for the Ammonia Decomposition Reaction. *Nat. Chem.*, *2* (2010), 484–489. doi: 10.1038/nchem.626.
- [33] Hansen, E. W. and Neurock, M. Modeling Surface Kinetics with First-Principles-Based Molecular Simulation. *Chem. Eng. Sci.*, *54* (1999), 3411–3421. doi: 10.1016/S0009-2509(98)00489-8.
- [34] Gokhale, A. A.; Dumesic, J. A.; and Mavrikakis, M. On the Mechanism of Low-Temperature Water Gas Shift Reaction on Copper. *J. Am. Chem. Soc.*, *130* (2008), 1402–1414. doi: 10.1021/ja0768237.
- [35] Van den Bossche, M. and Grönbeck, H. Methane Oxidation over PdO(101) Revealed by First-Principles Kinetic Modeling. *J. Am. Chem. Soc.*, *137* (2015), 12035–12044. doi: 10.1021/jacs.5b06069.

- [36] Trinchero, A.; Hellman, A.; and Grönbeck, H. Methane Oxidation over Pd and Pt studied by DFT and Kinetic Modeling. *Surf. Sci.*, *616* (2013), 206–213. doi: 10.1016/j.susc.2013.06.014.
- [37] Heard, C. J.; Hu, C.; Skoglundh, M.; Creaser, D.; and Grönbeck, H. Kinetic Regimes in Ethylene Hydrogenation over Transition-Metal Surfaces. *ACS Catal.*, *6* (2015), 3277–3286. doi: 10.1021/acscatal.5b02708.
- [38] Mei, D.; Du, J.; and Neurock, M. First-Principles-Based Kinetic Monte Carlo Simulation of Nitric Oxide Reduction over Platinum Nanoparticles under Lean-Burn Conditions. *Ind. Eng. Chem. Res.*, *49* (2010), 10364–10373. doi: 10.1021/ie100999e.
- [39] Loffreda, D.; Delbecq, F.; Vigné, F.; and Sautet, P. Catalytic Hydrogenation of Unsaturated Aldehydes on Pt(111): Understanding the Selectivity from First-Principles Calculations. *Angew. Chem. Int. Ed.*, *44* (2005), 5279–5282. doi: 10.1002/anie.200500913.
- [40] Yang, L.; Karim, A.; and Muckerman, J. T. Density Functional Kinetic Monte Carlo Simulation of Water-Gas Shift Reaction on Cu/ZnO. *J. Phys. Chem. C.*, *117* (2013), 3414–3425. doi: 10.1021/jp3114286.
- [41] Rogal, J.; Reuter, K.; and Scheffler, M. CO Oxidation on Pd(100) at Technologically Relevant Pressure Conditions: First-Principles Kinetic Monte Carlo study. *Phys. Rev. B*, *77* (2008), 155410. doi: 10.1103/PhysRevB.77.155410.
- [42] Piccinin, S. and Stamatakis, M. CO Oxidation on Pd(111): A First-Principles-Based Kinetic Monte Carlo Study. *ACS Catal.*, *4* (2014), 2143–2152. doi: 10.1021/cs500377j.
- [43] Kandoi, S.; Greeley, J.; Sanchez-Castillo, M. A.; Evans, S. T.; Gokhale, A. A.; Dumesic, J. A.; and Mavrikakis, M. Prediction of Experimental Methanol Decomposition Rates on Platinum from First Principles. *Top. Catal.*, *37* (2006), 17–28. doi: 10.1007/s11244-006-0001-1.
- [44] Schlögl, R. Heterogeneous Catalysis. *Angew. Chem. Int. Ed.*, *54* (2015), 3465–3520. doi: 10.1002/anie.201410738.
- [45] Österlund, L.; Grant, A. W.; and Kasemo, B. *Lithographic Techniques in Nanocatalysis*, chapter Lithographic Techniques in Nanocatalysis, pages 269–341. Springer Berlin Heidelberg, 2007. doi: 10.1007/978-3-540-32646-5.
- [46] Schauer mann, S. and Freund, H.-J. Model Approach in Heterogeneous Catalysis: Kinetics and Thermodynamics of Surface Reactions. *Acc. Chem. Res.*, *48* (2015), 2775–2782. doi: 10.1021/acs.accounts.5b00237.
- [47] Papp, C. From Flat Surfaces to Nanoparticles: In Situ Studies of the Reactivity of Model Catalysts. *Catal. Lett.*, *147* (2017), 2–19. doi: 10.1007/s10562-016-1925-0.
- [48] Freund, H.-J. Model Systems in Heterogeneous Catalysis: Selectivity Studies at the Atomic Level. *Top. Catal.*, *48* (2008), 137–144. doi: 10.1007/s11244-008-9052-9.

- [49] Zhdanov, V. P. and Kasemo, B. Monte Carlo Simulation of the Kinetics of Rapid Reactions on Nanometer Catalyst Particles. *Surf. Sci.*, *405* (1998), 27–37. doi: 10.1016/S0039-6028(97)01078-9.
- [50] Persson, H.; Thormählen, P.; Zhdanov, V. P.; and Kasemo, B. Monte Carlo Simulations of the Kinetics of Catalytic Reactions on Nanometer-Sized Particles, with Diffusion over Facet Boundaries. *J. Vac. Sci. Technol. A*, *17* (1999), 1721–1726. doi: 10.1116/1.581880.
- [51] Eyring, H. The Activated Complex and the Absolute Rate of Chemical Reactions. *Chem. Rev.*, *17* (1935), 65–77. doi: 10.1021/cr60056a006.
- [52] Mills, G.; Jónsson, H.; and Schenter, G. K. Reversible work Transition State Theory: Application to Dissociative Adsorption of Hydrogen. *Surf. Sci.*, *324* (1995), 305–337. doi: 10.1016/0039-6028(94)00731-4.
- [53] Kohanoff, J. *Electronic Structure Calculations for Solids and Molecules: Theory and Computational Methods*. Cambridge University Press, New York (USA), 2006.
- [54] Perdew, J. P.; Burke, K.; and Ernzerhof, M. Generalized Gradient Approximation Made Simple. *Phys. Rev. Lett.*, *77* (1996), 3865–3868. doi: 10.1103/PhysRevLett.77.3865.
- [55] Hammer, B.; Hansen, L. B.; and Nørskov, J. K. Improved Adsorption Energetics within Density-Functional Theory using Revised Perdew-Burke-Ernzerhof Functionals. *Phys. Rev. B*, *59* (1999), 7413–7421. doi: 10.1103/PhysRevB.59.7413.
- [56] Haas, P.; Tran, F.; and Blaha, P. Calculation of the Lattice Constant of Solids with Semilocal Functionals. *Phys. Rev. B*, *79* (2009), 085104. doi: 10.1103/PhysRevB.79.085104.
- [57] Blöchl, P. Projector Augmented-Wave Method. *Phys. Rev. B.*, *50* (1994), 17953–17979. doi: 10.1103/PhysRevB.50.17953.
- [58] Kittel, C. *Introduction to Solid State Physics*. John Wiley & Sons, Inc., Hoboken (USA), 8th edition edition, 2005.
- [59] Head, J. D. and Zerner, M. C. A Broyden–Fletcher–Goldfarb–Shanno Optimization Procedure for Molecular Geometries. *Chem. Phys. Lett.*, *122* (1985), 264–270. doi: 10.1016/0009-2614(85)80574-1.
- [60] Henkelman, G.; Uberuaga, B. P.; and Jónsson, H. A Climbing Image Nudged Elastic Band Method for Finding Saddle Points and Minimum Energy Paths. *J. Chem. Phys.*, *113* (2000), 9901–9904. doi: 10.1063/1.1329672.
- [61] Hoffmann, M. J.; Medford, A. J.; and Bligaard, T. Framework for Scalable Adsorbate–Adsorbate Interaction Models. *J. Phys. Chem. C*, *120* (2016), 13087–13094. doi: 10.1021/acs.jpcc.6b03375.

- [62] Van den Bossche, M. and Grönbeck, H. Adsorbate Pairing on Oxide Surfaces: Influence on Reactivity and Dependence on Oxide, Adsorbate Pair, and Density Functional. *J. Phys. Chem. C*, *121* (2017), 8390–8398. doi: 10.1021/acs.jpcc.6b12789.
- [63] Jansen, A. P. J. *An Introduction to Kinetic Monte Carlo Simulations of Surface Reactions*. Springer Berlin Heidelberg, 2012. doi: 10.1007/978-3-642-29488-4.
- [64] Gould, H. and Tobochnik, J. *Statistical and Thermal Physics With Computer Applications*. Princeton University Press, Woodstock, Oxfordshire, 2010. P 318.
- [65] Hill, T. L. *Introduction to Statistical Thermodynamics*. Dover Publications Inc., New York, 1986. Chapter 9.
- [66] Sprowl, L. H.; Campbell, C. T.; and Árnadóttir, L. Hindered Translator and Hindered Rotor Models for Adsorbates: Partition Functions and Entropies. *J. Phys. Chem. C*, *120* (2016), 9719–9731. doi: 10.1021/acs.jpcc.5b11616.
- [67] Jones, E.; Oliphant, T.; Peterson, P.; and et al. SciPy: Open source scientific tools for Python, 2001. URL <https://docs.scipy.org/doc/scipy/reference/tutorial/integrate.html>, [Online; accessed 2017-05-10].
- [68] Iserles, A. *A First Course in the Numerical Analysis of Differential Equations*. Cambridge University Press, second edition edition, 2009. Chapter 2 - Multistep Methods, [Books24x7 version] Available from <http://common.books24x7.com.proxy.lib.chalmers.se/toc.aspx?bookid=30922>.
- [69] Gillespie, D. T. A General Method for Numerically Simulating the Stochastic Time Evolution of Coupled Chemical Reactions. *J. Comput. Phys.*, *22* (1976), 403–434. doi: 10.1016/0021-9991(76)90041-3.
- [70] Chatterjee, A. and Vlachos, D. G. An Overview of Spatial Microscopic and Accelerated Kinetic Monte Carlo Methods. *J. Comput.-Aided Mater. Des.*, *14* (2007), 253–308. doi: 10.1007/s10820-006-9042-9.
- [71] Chatterjee, A. and Voter, A. F. Accurate Acceleration of Kinetic Monte Carlo Simulations through the Modification of Rate Constants. *J. Chem. Phys.*, *132* (2010), 194101. doi: 10.1063/1.3409606.
- [72] Fichthorn, K. A. and Lin, Y. A Local Superbasin Kinetic Monte Carlo Method. *J. Chem. Phys.*, *138* (2013), 164104. doi: 10.1063/1.4801869.
- [73] Puchala, B.; Falk, M. L.; and Garikipati, K. An Energy Basin Finding Algorithm for Kinetic Monte Carlo Acceleration. *J. Chem. Phys.*, *132* (2010), 134104. doi: 10.1063/1.3369627.
- [74] Dybeck, E. C.; Plaisance, C. P.; and Neurock, M. Generalized Temporal Acceleration Scheme for Kinetic Monte Carlo Simulations of Surface Catalytic Processes by Scaling the Rates of Fast Reactions. *J. Chem. Theory Comput.*, *13* (2017), 1525–1538. doi: 10.1021/acs.jctc.6b00859.

- [75] Zhu, G.; Han, J.; Zemlyanov, D. Y.; and Ribeiro, F. H. The Turnover Rate for the Catalytic Combustion of Methane over Palladium Is Not Sensitive to the Structure of the Catalyst. *J. Am. Chem. Soc.*, *126* (2004), 9896–9897. doi: 10.1021/ja049406s.
- [76] Zhu, G.; Han, J.; Zemlyanov, D. Y.; and Ribeiro, F. H. Temperature Dependence of the Kinetics for the Complete Oxidation of Methane on Palladium and Palladium Oxide. *J. Phys. Chem. B*, *109* (2005), 2331–2337. doi: 10.1021/jp0488665.
- [77] Monteiro, R.; Zemlyanov, D.; Storey, J. M.; and Ribeiro, F. H. Turnover Rate and Reaction Orders for the Complete Oxidation of Methane on a Palladium Foil in Excess Dioxygen. *J. Catal.*, *199* (2001), 291–301. doi: 10.1006/jcat.2001.3176.
- [78] Campbell, C. T. Future Directions and Industrial Perspectives Micro- and macrokinetics: their Relationship in Heterogeneous Catalysis. *Topics in Catalysis*, *1* (1994), 353–366. doi: 10.1007/BF01492288.
- [79] Stegelmann, C.; Andreasen, A.; and Campbell, C. T. Degree of Rate Control: How Much the Energies of Intermediates and Transition States Control Rates. *J. Am. Chem. Soc.*, *131* (2009), 8077–8082. doi: 10.1021/ja9000097.
- [80] McNaught, A. D. and Wilkinson, D. *IUPAC. Compendium of Chemical Terminology*. Blackwell Scientific Publications, Oxford, 2nd ed. (the "gold book") edition, 1997. [Online accessed 6th of April 2017 - <https://doi.org/10.1351/goldbook.O04322>].
- [81] G elin, P. and Primet, M. Complete Oxidation of Methane at Low Temperature over Noble Metal Based Catalysts: a Review. *Appl. Catal. B-Environ.*, *39* (2002), 1–37. doi: 10.1016/S0926-3373(02)00076-0.
- [82] Hoffund, G. B.; Li, Z.; Epling, W. S.; G obel, T.; Schneider, P.; and Hahn, H. Catalytic Methane Oxidation Over Pd Supported on Nanocrystalline and Polycrystalline TiO₂ Mn₃O₄, CeO₂ and ZrO₂. *React. Kinet. Catal. Lett.*, *70* (2000), 97–103. doi: 10.1023/A:1010362632223.
- [83] Hao, H.; Liu, Z.; Zhao, F.; and Li, W. Natural Gas as Vehicle Fuel in China: A Review. *Renewable Sustainable Energy Rev.*, *62* (2016), 521–533. doi: 10.1016/j.rser.2016.05.015.
- [84] Burch, R.; Loader, P.; and Urbano, F. Some Aspects of Hydrocarbon Activation on Platinum Group Metal Combustion Catalysts. *Catal. Today*, *27* (1996), 243–248. doi: 10.1016/0920-5861(95)00194-8.
- [85] Farrauto, R. J.; Hobson, M. C.; Kennelly, T.; and Waterman, E. M. Catalytic Chemistry of Supported Palladium for Combustion of Methane. *Appl. Catal. A-Gen.*, *81* (1992), 227–237. doi: 10.1016/0926-860X(92)80095-T.
- [86] Lundgren, E.; Gustafson, J.; Mikkelsen, A.; Andersen, J. N.; Stierle, A.; Dosch, H.; Todorova, M.; Rogal, J.; Reuter, K.; and Scheffler, M. Kinetic Hindrance during the Initial Oxidation of Pd(100) at Ambient Pressures. *Phys. Rev. Lett.*, *92* (2004), 046101. doi: 10.1103/PhysRevLett.92.046101.

- [87] Ketteler, G.; Ogletree, D. F.; Bluhm, H.; Liu, H.; Hebenstreit, E. L. D.; and Salmeron, M. In Situ Spectroscopic Study of the Oxidation and Reduction of Pd(111). *J. Am. Chem. Soc.*, *127* (2005), 18269–18273. doi: 10.1021/ja055754y.
- [88] Baldwin, T. R. and Burch, R. Catalytic Combustion of Methane over Supported Palladium Catalysts: II. Support and Possible Morphological Effects. *Appl. Catal.*, *66* (1990), 359–381. doi: 10.1016/S0166-9834(00)81649-8.
- [89] Hicks, R. F.; Qi, H.; Young, M. L.; and Lee, R. G. Structure Sensitivity of Methane Oxidation over Platinum and Palladium. *J. Catal.*, *122* (1990), 280–294. doi: 10.1016/0021-9517(90)90282-O.
- [90] Hicks, R. F.; Qi, H.; Young, M. L.; and Lee, R. G. Effect of Catalyst Structure on Methane Oxidation over Palladium on Alumina. *J. Catal.*, *122* (1990), 295–306. doi: 10.1016/0021-9517(90)90283-P.
- [91] Oh, S. H.; Mitchell, P. J.; and Siewert, R. M. Methane Oxidation over Alumina-Supported Noble Metal Catalysts With and Without Cerium Additives. *J. Catal.*, *132* (1991), 287–301. doi: 10.1016/0021-9517(91)90149-X.
- [92] Ciuparu, D.; Lyubovsky, M. R.; Altman, E.; Pfefferle, L. D.; and Datye, A. Catalytic Combustion of Methane over Palladium-based Catalysts. *Cat. Rev. - Sci. Eng.*, *44* (2002), 593–649. doi: 10.1081/CR-120015482.
- [93] Qi, W.; Ran, J.; Wang, R.; Du, X.; Shi, J.; and Ran, M. Kinetic Mechanism of Effects of Hydrogen Addition on Methane Catalytic Combustion over Pt(111) Surface: A DFT Study with Cluster Modeling. *Comp. Mater. Sci.*, *111* (2016), 430–442. doi: 10.1016/j.commatsci.2015.09.002.
- [94] Zhu, Y.-A.; Chen, D.; Zhou, X.-G.; and Yuan, W.-K. DFT Studies of Dry Reforming of Methane on Ni Catalyst. *Catal. Today.*, *148* (2009), 260–267. doi: 10.1016/j.cattod.2009.08.022.
- [95] Bligaard, T.; Nørskov, J. K.; Dahl, S.; Matthiesen, J.; Christensen, C. H.; and Sehested, J. The Brønsted–Evans–Polanyi Relation and the Volcano Curve in Heterogeneous Catalysis. *J. Catal.*, *224* (2004), 206–217. doi: 10.1016/j.jcat.2004.02.034.
- [96] Riedel, J. N.; Rötzer, M. D.; Jørgensen, M.; Vej-Hansen, U. G.; Pedersen, T.; Sebök, B.; Schweinberger, F. F.; Vesborg, P. C. K.; Hansen, O.; Schiøtz, J.; Heiz, U.; and Chorkendorff, I. H₂/D₂ Exchange Reaction on Mono-Disperse Pt Clusters: Enhanced Activity from Minute O₂ Concentrations. *Catal. Sci. Technol.*, *6* (2016), 6893–6900. doi: 10.1039/C6CY00756B.
- [97] Campbell, C. T.; Ertl, G.; Kuipers, H.; and Segner, J. A Molecular Beam Study of the Catalytic Oxidation of CO on a Pt(111) surface. *J. Chem. Phys.*, *73* (1980), 5862–5873. doi: 10.1063/1.440029.
- [98] Park, J. Y.; Zhang, Y.; Grass, M.; Zhang, T.; and Somorjai, G. A. Tuning of Catalytic CO Oxidation by Changing Composition of Rh-Pt Bimetallic Nanoparticles. *Nano Lett.*, *8* (2008), 673–677. doi: 10.1021/nl073195i.

- [99] Nakao, K.; Watanabe, O.; Sasaki, T.; Ito, S.-I.; Tomishige, K.; and Kunimori, K. CO Oxidation on Pd(111), Pt(111), and Rh(111) Surfaces studied by Infrared Chemiluminescence Spectroscopy. *Surf. Sci.*, *601* (2007), 3796–3800. doi: 10.1016/j.susc.2007.04.015.
- [100] Palmer, R. L. and Smith Jr., J. N. Molecular Beam Study of CO Oxidation on a (111) Platinum Surface. *J. Chem. Phys.*, *60* (1974), 1453–1463. doi: 10.1063/1.1681219.
- [101] Gerrard, A. L. and Weaver, J. F. Kinetics of CO Oxidation on High-Concentration Phases of Atomic Oxygen on Pt(111). *J. Chem. Phys.*, *123* (2005), 224703. doi: 10.1063/1.2126667.
- [102] Vogel, D.; Spiel, C.; Suchorski, Y.; Trincherro, A.; and Schlögl, R. Local Catalytic Ignition during CO Oxidation on Low-Index Pt and Pd Surfaces: A Combined PEEM, MS, and DFT Study. *Angew. Chem., Int. Ed.*, *51* (2012), 10041–10044. doi: 10.1002/anie.201204031.
- [103] Wrobel, R. J.; Becker, S.; and Weiss, H. Second/Additional Bistability in a CO Oxidation Reaction on Pt(111): An Extension and Compilation. *J. Phys. Chem. C*, *116* (2012), 22287–22292. doi: 10.1021/jp302270n.
- [104] Völkening, S. and Wintterlin, J. CO Oxidation on Pt(111) - Scanning Tunneling Microscopy Experiments and Monte Carlo Simulations. *J. Chem. Phys.*, *114* (2001), 6382–6395. doi: 10.1063/1.1343836.
- [105] Calderón, S. K.; Grabau, M.; Óvári, L.; Kress, B.; Steinrück, H.-P.; and Papp, C. CO Oxidation on Pt(111) at Near Ambient Pressures. *J. Chem. Phys.*, *144* (2016), 044706. doi: 10.1063/1.4940318.
- [106] Alavi, A.; Hu, P.; Deutsch, T.; Silvestrelli, P. L.; and Hutter, J. CO Oxidation on Pt(111): An Ab Initio Density Functional Theory Study. *Phys. Rev. Lett.*, *80* (1998), 3650–3653. doi: 10.1103/PhysRevLett.80.3650.
- [107] Cheng, Z.; Fine, N. A.; and Lo, C. S. Platinum Nanoclusters Exhibit Enhanced Catalytic Activity for Methane Dehydrogenation. *Top. Catal.*, *55* (2012), 345–352. doi: 10.1007/s11244-012-9803-5.

